Deep–Sea Research II 206 (2022) 105214

Contents lists available at ScienceDirect

Deep-Sea Research Part II

journal homepage: www.elsevier.com/locate/dsr2

# High-resolution biological net community production in the Pacific-influenced Arctic as constrained by $O_2/Ar$ and $O_2/N_2$ observations

Haley Cynar [a,*], Lauren W. Juranek [a], Calvin W. Mordy [b,c], David Strausz [b,c], Shaun Bell [c]

[a] College of Earth, Ocean, and Atmospheric Sciences, Oregon State University, Corvallis, USA
[b] Cooperative Institute for Climate, Ocean, and Ecosystem Studies, University of Washington, Seattle, USA
[c] Pacific Marine Environmental Laboratory, National Oceanic and Atmospheric Administration, Seattle, USA

ARTICLE INFO

*Keywords:*
$O_2/Ar$
$O_2/N_2$
Dissolved gases
Gas tension device
Primary productivity
Net community production
Pacific Arctic

ABSTRACT

Spatial and temporal patterns of primary productivity in the Arctic are expected to change with warming-associated changes in ice cover and stratification, yet productivity measurements are historically spatially and temporally limited. Over the last two decades, an approach that uses measurement of dissolved oxygen/argon ratios ($O_2/Ar$) from a vessel's underway seawater system has emerged as an established method to assess net community production (NCP) rates with high spatial and/or temporal resolution. More recently, the measurement of oxygen/nitrogen ratios ($O_2/N_2$) with a gas tension device (GTD) and optode have been piloted in underway settings to provide comparable NCP estimates. The GTD/optode approach has several advantages: instrumentation is small, inexpensive, and suitable for autonomous deployments; however, dissimilarity in solubility between $O_2$ and $N_2$ makes this tracer pair less accurate than $O_2/Ar$. We conducted a side-by-side ship-based comparison of a GTD/optode and Equilibrator Inlet Mass Spectrometer (EIMS) in the Pacific Arctic during one of the North Pacific Research Board Integrated Ecosystem Research Program cruises in 2019. NCP from $O_2/Ar$ and $O_2/N_2$ approaches were coherent throughout this cruise, with median mixed layer integrated NCP of 9.3 $\pm$ 2.8 and 7.9 $\pm$ 3.2 mmol $O_2$ $m^{-2}$ $day^{-1}$, respectively. The range of NCP was large, from less than zero to >100 mmol $O_2$ $m^{-2}$ $day^{-1}$, with some of the largest NCP estimates measured at well-established hotspots in the Pacific Arctic. While $O_2/Ar$ and $O_2/N_2$ largely tracked each other, deviations were observed, principally in the Bering Sea where wind-induced bubbles were a primary driver, while a combination of temperature and wind drove differences over the majority of the cruise. The GTD/optode can be used to enhance spatial and temporal coverage of NCP measurements, yet the uncertainty makes this approach better-suited to regions with higher overall rates of NCP, while regions near-equilibrium may result in unacceptably high uncertainty. Additionally, the GTD/optode is reliant on well-calibrated oxygen observations, a potential challenge if autonomously deployed.

## 1. Introduction

The Arctic Ocean is changing at an unprecedented rate: the thirteen lowest minimum sea ice extents in the satellite record have all occurred between 2007 and 2020, while the trend in September sea ice extent has been declining by 13.3% per decade over the period 1979–2014, relative to the mean September sea ice extent from 1981 to 2010 (Serreze and Stroeve 2015; Stroeve and Meier 2018; Andersen et al., 2020). In some of the most impacted regions of the Arctic Ocean, including the Chukchi and western Beaufort seas, the ice season duration has been declining by an average of 2.8 days per year from 1979/1980 to 2010/2011 (Stammerjohn et al., 2012). This rapid decline in sea ice impacts the physical environment in many ways: increased exchange of heat and gases ($CO_2$) across the air-sea boundary (Anderson and Kaltin 2001; Carmack et al., 2015; Danielson et al., 2020; DeGrandpre et al., 2020), enhanced wind fetch across open water that results in greater waves (Thomson and Rogers 2014), and greater stratification from low-salinity meltwater (Toole et al., 2010). Stronger stratification limits vertical mixing, which in turn limits surface nutrient supply, a fundamental requirement for photosynthesis (Semiletov et al., 2004; Carmack and Wassmann 2006; Song et al., 2021).

The impact of these physical changes on primary productivity is

* Corresponding author.
*E-mail address:* cynarh@oregonstate.edu (H. Cynar).

https://doi.org/10.1016/j.dsr2.2022.105214
Received 28 February 2022; Received in revised form 15 September 2022; Accepted 27 October 2022
Available online 8 November 2022

uncertain, with hypotheses for both increasing and decreasing production based on nutrient and light availability. Remote sensing studies have indicated an increase in primary production, driven by sea ice loss and reduction in light limitation (Arrigo et al., 2008; Tremblay et al., 2011; Arrigo and van Dijken 2015), although these studies acknowledge a requirement for increased nutrient flux to maintain production. This influx of nutrients could be sustained by increased supply by circulation from adjacent subpolar seas to the Arctic through "inflow" shelves (Carmack and Wassmann 2006) which are situated at Arctic gateways. The Chukchi Sea is one such inflow shelf where nutrient-rich Pacific-origin water from the Bering Sea shoals through Bering Strait onto the Chukchi shelf. Due to this influx, inflow shelves like the Chukchi are expected to be most impacted by physical changes that enhance nutrient supply from neighboring seas (Tremblay and Gagnon 2009; Tremblay et al., 2015; Lewis et al., 2020). Alternatively, potential increases in cloud cover are expected to decrease production (Bélanger et al., 2013), while increased delivery of freshwater and dissolved constituents from terrestrial snow, ice, and permafrost melt via Arctic rivers will impact nutrients, stratification, and organic matter in coastal regions with variable results (Carmack and Wassmann 2006). Overall, a melting Arctic Ocean will alter surface light and nutrient availability on a seasonal basis, effectively controlling phytoplankton growth, and thus carbon and energy cycling in Arctic marine food webs (Grebmeier et al., 2006; Harada 2016). These shifts are best understood through a multidisciplinary approach, as with the North Pacific Research Board Arctic Integrated Ecosystem Research Program (https://www.nprb.org/arctic-program; Baker et al., 2020, 2022, this issue).

While remote sensing approaches are one of the best tools for providing spatially and temporally resolved estimates of marine primary productivity, passive measurements (e.g., ocean color) are often limited in some seasons and regions of the Arctic due to cloud cover, especially during the late ice-free season (August–October) when physical system changes exhibit strong trends. Additionally, satellite-based estimates of net community productivity (NCP) are not yet widely available in the Pacific Arctic region. An important productivity metric, NCP is defined as the total community photosynthesis less both algal and heterotrophic respiration, and is considered to be an estimate of the maximum organic carbon available to be exported out of the surface ocean, with implications for the ecosystem, fisheries, carbon budgets, and climate modeling (Wassmann and Reigstad 2011). Since biological production in shallow, marginal seas like the Chukchi can be dynamic, with patchy and short-lived phytoplankton blooms (Juranek et al., 2019), higher resolution methods are needed to capture sporadic and spatially-variable processes in the field and to understand potential drivers of these patterns.

In the last two decades, a number of studies have shown the utility of high-resolution observations of surface ocean dissolved oxygen/argon ($O_2$/Ar) gas ratios to constrain NCP at spatial and or temporal scales that are not accessible with traditional incubation methods (e.g., Hamme et al., 2012; Eveleth et al., 2017; Juranek et al., 2019). High-resolution $O_2$/Ar can be obtained continuously in surface seawater using an equilibrated inlet mass spectrometer (EIMS) (Cassar et al., 2009). Since Ar is an inert gas that is not affected by biology but behaves similarly to $O_2$ with respect to physical forcing, it can be used to isolate the biological effects driving $O_2$ (Benson and Krause 1984; Craig and Hayward 1987). The ratio of biologically and physically controlled $O_2$ to physically controlled Ar therefore can be used to provide an estimate of net biological oxygen production (Kaiser et al., 2005). The $O_2$/Ar ratio is insensitive to changes due to warming, cooling, and wind-driven bubble exchange and injection due to the similarity in physical properties between oxygen and argon. When $O_2$/Ar measurements are combined with a mass-balance budget for the surface ocean, spatially resolved estimates of NCP can be produced (e.g., Stanley et al., 2010; Hamme et al., 2012; Eveleth et al., 2017; Teeter et al., 2018).

Another related, but less frequently used approach for obtaining NCP is to use observations of the $O_2$/$N_2$ ratio in seawater. Similar to the case with $O_2$/Ar, $N_2$ is used to track abiotic forcing. However, while $O_2$ and Ar are an ideal tracer pair due to the similar solubility of these gases, the solubility of $N_2$ is less similar to $O_2$, and is impacted differently by both physical forcing (i.e., warming, cooling, and bubbles) (Hamme et al., 2019) and, at times, biological influences (i.e., nitrogen fixation and denitrification).

$O_2$/$N_2$ measurements were previously described by Emerson et al. (2002), who used observations from a mooring in the subtropical North Pacific to estimate net biological oxygen production. The approach involves measuring total gas pressure as well as $pO_2$ in seawater with a gas tension device (GTD) and $O_2$ sensor, respectively, with assumptions about less prevalent gases to estimate the amount of dissolved $N_2$. Because of the reliance on $O_2$ to calculate $N_2$, the approach requires accurate dissolved $O_2$ concentrations (Emerson et al., 2002).

GTD measurements were first tested on moorings (McNeil et al., 1995) and have since been broadly applied (Emerson et al., 2002, 2008, 2019; Weeding and Trull 2014; Trull et al., 2019), while continuous shipboard GTD measurements have also been made to estimate $O_2$/$N_2$-based net biological oxygen production (McNeil et al., 2005). Recently, Izett and Tortell (2020) introduced a GTD and optode configuration (Pressure of In Situ Gases Instrument, or PIGI) for deployment on underway systems, with initial data collection in the northeast Pacific and Canadian Arctic oceans.

While $O_2$/$N_2$-based net biological oxygen estimates are subject to greater biases and uncertainties due to the dissimilarities in physical forcing of $O_2$ and $N_2$, there are also key advantages to the approach. The GTD/optode system is small, submersible, and low-cost, with potential for autonomous use, whereas the EIMS involves a more expensive, ship-based mass spectrometer that requires supervision.

Here, we compare underway $O_2$/$N_2$ measured by GTD/optode to the more established $O_2$/Ar method measured by EIMS (Stanley et al., 2010; Hamme et al., 2012; Lockwood et al., 2012; Eveleth et al., 2014) to (1) Compare $O_2$/$N_2$ to $O_2$/Ar; (2) estimate the uncertainties of each method; 3) quantify the spatial variability in NCP; 4) evaluate physical drivers of NCP in this region of the Pacific Arctic.

### 1.1. Basis of $O_2$/Ar and $O_2$/$N_2$ approach

Biological $O_2$ production can be stoichiometrically related to the net inventory of organic carbon produced through the balance of community photosynthesis and respiration, i.e.: $CO_2 + H_2O \leftrightarrow$ organic matter $+ O_2$. As is evident from this expression, net biological oxygen increases (decreases) due to photosynthesis (respiration) in a given parcel of water. However, background concentrations of $O_2$ in surface seawater are set by temperature- and salinity-controlled solubility (Garcia and Gordon, 1992). Therefore, deviations from solubility equilibrium, identified by the dissolved gas saturation anomaly of oxygen in the surface ocean:

$$\Delta O_2\ (\%) = 100*([O_2]_{meas}/[O_2]_{sat} - 1) \quad (1)$$

where $[O_2]_{meas}$ is the measured oxygen concentration and $[O_2]_{sat}$ is the equilibrium oxygen solubility, are due to a combination of recent biological and physical forcing. For example, a recent water column warming of 3°C (e.g., from 10°C to 13°C, S = 32) without sufficient time for re-equilibration with the atmosphere would increase $\Delta O_2$ by 6.57% due to the decrease in solubility of $O_2$ ($[O_2]_{sat}$) with increasing temperature. A positive gas saturation anomaly could also be driven by a source of $O_2$ (i.e., photosynthesis), which increases $[O_2]_{meas}$. Without an additional tracer gas, it is difficult to identify when positive $\Delta O_2$ are driven by biological production or a combination of physical factors. By simultaneously measuring an abiotic gas such as Ar or $N_2$ as a tracer of physical saturation changes, the physical and biological components of the $\Delta O_2$ signal can be parsed out. Ar has been widely used as an abiotic tracer alongside $O_2$ because it is inert and is physically similar to oxygen (Craig and Hayward 1987). Although $N_2$ has biological sources and

sinks, the effect of these processes are undetectable given the large $N_2$ background in surface measurements, making $N_2$ an effective tracer of physical processes (Emerson et al., 2002). With Ar and $N_2$ serving as proxies for physical gas saturation, the normalization of $\Delta O_2$ relative to either gas yields a tracer of the net biological oxygen saturation (Kaiser et al., 2005).

The physical differences between $N_2$ and $O_2$ are significantly greater than those between Ar and $O_2$, so physical forcing (for example, warming or cooling of water masses) is expected to drive slightly different responses in $O_2$ and $N_2$, and hence the $O_2/N_2$ ratio will not be a perfect tracer of net biological $O_2$ production. Since $N_2$ makes up 78% of the atmosphere (Glueckauf 1951) yet is less soluble in seawater than either $O_2$ or Ar, the effect of bubble injection increases $N_2$ saturation significantly more than $O_2$ or Ar. The effect of temperature change on $N_2$, in contrast, is smaller than that of $O_2$ and Ar, which also biases the ratio when temperature change is observed.

To account for the physical biases of $N_2$, Izett et al. (2021) introduced a calculated value, $N_2$', which more closely approximates a physical analogue of oxygen, improving upon the approximation of net biological oxygen production based on $O_2/N_2$ in some regions. We explored the utility of this $N_2$' approach in our study region by comparing $O_2/N_2$ and $O_2/N_2$' with $O_2$/Ar observations.

## 2. Methods

In this study, EIMS- and GTD-based estimates of NCP were obtained for a side-by-side comparison on leg 1 of the OS1901 cruise (August 1 to August 24, 2019), part of the North Pacific Research Board's Arctic Integrated Ecosystem Research Program (Baker et al., 2020, 2022) in the Chukchi and Beaufort Seas, on R/V *Ocean Starr*. Leg 1 of the cruise embarked from Dutch Harbor, AK and ended in Nome, AK.

### 2.1. Dissolved $O_2$ measurements

An Aanderaa optode (4330 F) was placed in-line with the GTD in the flowthrough seawater system, which had a nominal intake depth of 3.5 m. The optode was calibrated from discrete samples that were collected periodically throughout the cruise (n = 26), and analyzed using the Winkler method (Carpenter 1965). Upon inspection, 5 of these samples were determined to be outliers (offset >2 $\sigma$ from mean or were analyzed in a batch of samples that were subject to analysis error); these outliers were excluded from further analysis. Oxygen gain (Winkler $O_2$/optode $O_2$) was determined with respect to time, temperature, and oxygen concentration, where the best fit linear model of the difference in gain correction as a function of time ($R^2$ = 0.58) was applied to the data (Fig. S1, Supplemental Information). This time-based gain correction ranged from 1.034 to 1.051 and is described in the Supplemental Information.

### 2.2. EIMS-$O_2$/Ar

An EIMS, which consists of a quadrupole mass spectrometer (Pfeiffer PrismaPlus QMG 220) coupled to a system for separation of dissolved gases from seawater, was configured similarly to that described by Cassar et al. (2009). $O_2$/Ar ratios were continuously measured on surface seawater by the EIMS, where seawater passed through a 40 mesh (0.42 mm) coarse screen into an overflowing cylinder in a sipper system. Seawater near the inflow of this cylinder was pumped through 100 μm and 5 μm filters and then passed through a contactor membrane (3 M Liqui-cel MicroModule 0.75 × 1, model G569) with large surface area in which dissolved gases equilibrated. The headspace of gas in this contactor membrane was sampled by a fused silica capillary (2 m × 0.05 mm ID) connected to the quadrupole mass spectrometer. A changeover valve allowed outside air to be admitted for 30 min every 3 h. The $O_2$/Ar in ambient air is considered to be constant, so consistent air measurements throughout the cruise allows for calibration of the seawater $O_2$/Ar signal to air $O_2$/Ar to account for potential drift in EIMS measurements over time.

The EIMS $O_2$/Ar ratios were time-averaged into 2.5-min intervals to yield measurements with average spatial resolution of ca. 0.6 km along the ship transit. EIMS-based $O_2$/Ar measurements are slightly lagged relative to faster response $O_2$ optode data due to equilibration and capillary transport time. Using a cross-correlation analysis, an EIMS-to-optode lag of 8.5 min was identified, and the EIMS time axis was shifted accordingly to align with the faster response optode data. Bottle samples were collected from the underway seawater stream twice a day and analyzed via a shore-based Thermo 253 Isotope Ratio Mass Spectrometer (IRMS) as in Juranek et al. (2012). Bottle samples were used as a secondary, external accuracy check on air corrected EIMS $O_2$/Ar. Outliers in the bottle calibrations (offset >3 $\sigma$ from mean difference) were observed in frontal regions of rapid $O_2$/Ar ratio change, and were excluded from comparison because small differences in sampling response time allowed for large offsets between EIMS and bottle $O_2$/Ar that were inconsistent with the majority of the data. Bottle and EIMS $O_2$/Ar data were used with paired temperature and salinity to calculate the $O_2$/Ar saturation anomaly ($\Delta O_2$/Ar) as follows:

$$\Delta O_2/Ar = 100*[\ (O_2/Ar)_{meas}/(O_2/Ar)_{sat}\text{-}1], \quad (2)$$

where $(O_2/Ar)_{sat}$ refers to the ratio of gases at saturation in seawater and $O_2$ and Ar solubilities are calculated according to Garcia and Gordon (1992) and Hamme and Emerson (2004), respectively. We observed a consistent, stable offset between EIMS and bottle sample $\Delta O_2$/Ar of −1.33% (n = 34, s. e.m. = 0.1%). The discrete bottle sampling occurred at the same sink where the EIMS sipper system was sampling from, such that no difference in warming or potential respiration in the lines (Juranek and Quay 2010) is expected to have led to this difference. A 5% difference in the EIMS total pressure between air and equilibrator measurements was attributed to slight differences in PEEK tubing length; because the gas ratio measurements are affected by total gas pressure in the quadrupole mass spectrometer this difference likely contributed to the offset correction required for $\Delta O_2$/Ar on this cruise. We adjusted all EIMS data to correct for this offset. See metadata description accompanying archived data at arcticdata. io (https://doi.org/10.18739/A2319S41N) for further details.

### 2.3. GTD-$O_2/N_2$

The Pro-Oceanus miniTDGP (referred to as GTD) was installed on the flowthrough seawater system to measure total dissolved gas pressure of surface seawater throughout the cruise. This device measures the total dissolved gas pressure across a permeable membrane twice per second. The flow rate of seawater entering the GTD was about 1.2 L $min^{-1}$, which yielded measurements with a faster response time than the EIMS. The underway seawater was split between the sensor wall (where the TDGP was located) and the EIMS tap, which had a split valve for discrete sampling. Since this TDGP configuration was set up directly in line with the underway seawater (in contrast to the EIMS with a sipper), these measurements were subject to greater noise at times due to bubbles in the seawater line, despite being adjacent to the EIMS seawater sampling location.

The GTD measures total dissolved gas pressure in seawater ($P^w_{GTD}$) expressed as in Eq. (3),

$$P^w_{GTD} = P^w_{N2} + P^w_{O2} + P^w_{H20} + P^w_{Ar} + P^w_{CO2} \quad (3)$$

where $P^w_x$ refers to the partial pressure of dissolved $N_2$, $O_2$, water vapor, Ar, and $CO_2$ in seawater, respectively. This expression excludes gases with partial pressures less than 20 μatm, which Emerson et al. (2002) showed was a reasonable assumption. $P^w_{Ar}$, $P^w_{CO2}$, and $P^w_{H2O}$ are assumed to be at equilibrium with the atmosphere, an assumption that is likely inaccurate, yet expected deviations in these gas concentrations will not strongly affect the calculation due to the small contribution of each of

these gases to total dissolved gas pressure. Alternately, the saturation of Ar can be assumed to be equal to $N_2$ in the calculation based on roughly similar saturations from physical forcing (McNeil et al., 2005). In this study, we assume $P^w_{Ar}$ to be in equilibrium with the atmosphere, but we investigate the impact of these assumptions in Section 3.2. The dry air mole fraction of $CO_2$ in the atmosphere was used in this calculation, where the monthly average $pCO_2$ in August 2019 at the Point Barrow, AK climate monitoring station was 400 ppm (NOAA CMDL, Table 1). The partial pressure of $CO_2$ and Ar were calculated based on the mole fraction of each gas in the atmosphere with the relationship in Eq. (4):

$$P^a_i = X_i*(P^a - P^a_{H20}) \quad (4)$$

where $P^a_i$ is the partial pressure of gas (i = $CO_2$ or Ar), $X_i$ is the fraction of gas in a dry atmosphere ($X_{Ar}$ = 0.00934; $X_{CO2}$ = 0.000400), $P^a$ is the atmospheric mean sea level pressure (in mbar) from NARR reanalysis products (Table 1) and $P^a_{H2O}$ is the partial pressure of water vapor in the atmosphere (Glueckauf 1951). $P^w_{H2O}$ is assumed to be at saturation in the GTD headspace and is calculated with the formula of Weiss and Price (1980), as in Eq. (5).

$$P^w_{H20} = 1013.25*\exp(24.4543–67.4509*(100/T_{abs}) - 4.8489*\log(T_{abs}/100) - 5.44E\text{-}4*S) \quad (5)$$

The equilibrium saturation concentration of oxygen at each location, $[O_2]_{sat}$, was determined based on the equations of Garcia and Gordon (1992). The partial pressure of dissolved oxygen, $P^w_{O2}$, was calculated from oxygen concentration ($[O_2]$, μmol $L^{-1}$) using an adaptation of Equation E from Bittig et al. (2018),

$$P^w_{O2} = [O_2] * \frac{X_{O2} * \left(1013.25–P^a_{H2O}\right)}{T_{corr}*S_{corr}}; \quad (6)$$

where the 1013.25 term is for standard atmospheric pressure (mbar), $P^a_{H2O}$ is the partial pressure of water vapor in the atmosphere (in mbar, assumed to be at saturation) and $X_{O2}$ is the mole fraction of $O_2$ in a dry atmosphere (0.20946, Glueckauf 1951). $T_{corr}$ and $S_{corr}$ are the temperature and salinity correction factors (Benson and Krause 1984; Garcia and Gordon 1992). The original equation contains an exponential term to account for water pressure, which was omitted here due to the hydrostatic pressure of zero, cancelling this term out.

$P^w_{N2}$ can then be calculated as in Emerson et al., (2002):

$$P^w_{N2} = P^w_{GTD} - (P^a–P^a_{H20})*(X_{Ar} + X_{CO2}) - P^w_{H20} - P^w_{O2}; \quad (7)$$

where $P^a$ is the atmospheric mean sea level pressure from NARR reanalysis products (Table 1). The $P^w_{GTD}$ data were time-shifted to account for a 1-min GTD-to-optode lag (determined via a cross-correlation analysis of the entire dataset, see metadata description accompanying archived data for further details; https://doi.org/10.18739/A2Z892G7H) relative to the faster response Aanderaa optode data, a response time that is within the range of comparable systems (Izett and Tortell 2020). The flow was manually maintained at 1.2 L $min^{-1}$ and flow rate was not recorded. Slight variations in flow may have caused slight variations in the response time but these are not likely to influence our interpretation of the data. From $P^w_{N2}$ and $P^w_{O2}$ as calculated post-$P^w_{GTD}$ lag correction, measured $O_2/N_2$ ratios were determined.

We report $O_2/N_2$ here in terms of a saturation anomaly ratio comparable to Eq. (2):

$$\Delta O_2/N_2\ (\%) = 100*[\ (O_2/N_2)_{meas}/(O_2/N_2)_{sat} - 1] \quad (8)$$

where $(O_2/N_2)_{sat}$ refers to the ratio of gases at saturation in equilibrium with the GTD headspace as calculated by Eqs. (6) and (7). The gas solubilities are calculated from Garcia and Gordon (1992) and Hamme and Emerson (2004). After calculating the $O_2/N_2$ ratio, a median residual filter was applied to remove outliers and noise due to in-line bubbles. A moving median was calculated based on a 12-min window, with residuals outside of 2.4 standard deviations from the mean flagged as outliers. These outliers were removed from the data, where this threshold was determined to exclude less than 5% of the data. This filtered version of $O_2/N_2$ is used throughout this manuscript and is referred to as noise-filtered (n.f.). See metadata description accompanying archived data at arcticdata.io (https://doi.org/10.18739/A2Z892G7H) for further details.

**Table 1**
Environmental data descriptions, resolution, and sources.

| Data type | Resolution | Source | URL |
|---|---|---|---|
| Directional wind speed at 10 m | 3-hourly, 0.3 deg | NCEP North American Regional Reanalysis (NARR); NOAA/OAR/ESRL PSL, Boulder, Colorado, USA | https://psl.noaa.gov/data/gridded/data.narr.html |
| Atmospheric pressure at mean sea level | Daily, 0.3 deg | NCEP North American Regional Reanalysis (NARR); NOAA/OAR/ESRL PSL, Boulder, Colorado, USA | https://psl.noaa.gov/data/gridded/data.narr.html |
| Sea surface temperature (SST) | Daily, 0.25 deg | NOAA High-resolution 360 Blended Analysis of Daily SST and Ice data; NOAA/OAR/ESRL PSL, Boulder, Colorado, USA | https://psl.noaa.gov/ |
| Sea ice concentration | Daily, 0.25 deg | NOAA High-resolution 360 Blended Analysis of Daily SST and Ice data; NOAA/OAR/ESRL PSL, Boulder, Colorado, USA | https://psl.noaa.gov/ |
| $pCO_2$ at Point Barrow, AK | Monthly | NOAA Climate Monitoring and Diagnostics Laboratory (CMDL) | https://www.esrl.noaa.gov/gmd/dv/data |
| Chlorophyll-a | Daily, 4 km | NASA Goddard Space Flight Group; Ocean Ecology Laboratory; Ocean Biology Processing Group | https://modis.gsfc.nasa.gov/data/ |

### 2.4. Comparison of $O_2/Ar$ and $O_2/N_2$ data

To assess the difference between $O_2/Ar$ and $O_2/N_2$ ratios, we calculate the term diff-Δ:

$$\text{diff-}\Delta\ (\%) = \Delta O_2/Ar - \Delta O_2/N_2 \quad (9)$$

Initially, to get more directly comparable $\Delta O_2/Ar$ - $\Delta O_2/N_2$, we tried to account for the dynamic response effects of the EIMS. The EIMS equilibrator uses a contactor membrane that dampens the signal due to the time required for gases to reach equilibrium across the membrane. When calculating diff-Δ, the comparatively slower response of the EIMS relative to the GTD creates data artifacts due to mismatched peaks. In an attempt to account for smearing of signals within the EIMS equilibrator, smoothed versions of $\Delta O_2/N_2$ were calculated, but neither a time filter (as in Hamme et al., 2015), nor a one-sided exponential filter with e-folding time comparable to that described by Cassar et al. (2009) for EIMS system response, closely approximated the smoothing effect of the EIMS contactor membrane. Because of this inability to slow down the GTD observations in a way that was directly comparable to the EIMS we decided to directly compare the GTD and EIMS records instead, and to flag areas where rapid changes in $O_2/Ar$ and $O_2/N_2$ caused large diff-Δ that are likely an artifact of differential dynamic responses.

### 2.5. NCP calculation

NCP was calculated for $\Delta O_2/Ar$ and $\Delta O_2/N_2$ values by assuming a steady-state balance between net biological oxygen production and air-sea gas exchange in the surface mixed layer with no horizontal advection or vertical mixing of water masses (Craig and Hayward 1987; Kaiser et al., 2005; Hamme and Emerson 2006; Stanley et al., 2010). When

there is physical transport of deeper water to the surface and mixing assumptions are invalidated it is not appropriate to calculate NCP using this steady-state balance (Teeter et al., 2018). Diagnosing potential mixing biases using only surface underway data can be challenging, but some characteristics of deeper water that may indicate vertical mixing in the region of this study include elevated salinity coupled with negative $\Delta O_2/Ar$ at the surface, since subsurface waters are typically depleted in oxygen at depth due to respiration, and their salinity is higher due to minimal influence of seasonal ice melt at depth. In this dataset, areas with both a $\Delta O_2/Ar$ less than −2% and a surface salinity greater than 32.5 (where the mean surface salinity over the cruise was 30.6, with less than 5% of measurements greater than 32.5) are assumed to be subject to vertical mixing, and are excluded from NCP analysis.

NCP based on the surface mass balance (Hendricks et al., 2004; Juranek and Quay 2005) was calculated using Eq. (10) with NCP in mmol $O_2$ $m^{-2}$ $day^{-1}$:

$$NCP = (k_{O2})\ (O_2)_{sat}(\Delta O_2/[X])/100, \quad (10)$$

In Eq. (10), $k_{O2}$ is the air-sea gas exchange rate (m $day^{-1}$), $(O_2)_{sat}$ is the equilibrium saturation of oxygen calculated as described above (mmol $m^{-3}$), and $\Delta O_2/[X]$ is either $\Delta O_2/Ar$ or $\Delta O_2/N_2$ as calculated with Eq. (2) or 8. The gas transfer velocity, $k_{O2}$, is dependent on wind speed and was calculated based on Wanninkhof (2014) using the wind speed weighting technique of Reuer et al. (2007), assuming a constant 20 m mixed layer depth (MLD). The MLD observed at the time of sampling fluctuated regionally throughout this cruise, with deeper MLDs in the Bering Sea and shallower (<15 m) MLD in the Chukchi and Beaufort Seas, as determined by the pycnocline depth. The MLD in these areas may have also varied in the weeks prior to sampling, such that an estimate of 20 m is a reasonable approximation with some uncertainty based on the historical MLD. In areas with shallower MLDs, the assumed 20 m MLD results in an overestimate of $k_{O2}$ of about 3%, while areas with deeper MLDs result in an underestimate of less than 1% in $k_{O2}$, biases which propagate into NCP estimates. Wind speed data were used in calculating the gridded wind speed for the 60 days prior to ship observations (Table 1).

### 2.6. Variables to assess physical gas saturation

To evaluate potential variables that might correlate with differences in $O_2/Ar$ and $O_2/N_2$ ratios, we compare remotely sensed wind speed and temperature to diff-Δ. Table 1 summarizes the data sources referenced throughout this text. The 3-h wind speed from NCEP North American Regional Reanalysis (NARR) products (Mesinger et al., 2006, Table 1) was used in calculating the maximum wind speed over the two preceding weeks, as well as the percent of wind speeds exceeding 10 m $s^{-1}$ over prior weeks. Net temperature change was calculated as the sum of daily sea surface temperature (SST) change 14 and 30 days prior to sampling using daily SST data (Table 1) collocated with the cruise track.

### 2.7. N2' calculations

$N_2$' is a value which approximates a physical analogue of oxygen, and is determined with a model developed by Izett and Tortell (2021) that is based on the historical physical forcing (wind, temperature, atmospheric pressure, sea ice) in combination with measured $N_2$ saturation to correct for biases. When using this model in calculating $N_2$' for this cruise (Izett, 2021), 3-h average directional components of wind speed and daily atmospheric pressure at mean sea level from NARR (Table 1) were used in calculating the historical wind speed and atmospheric pressure collocated with the cruise track for the 90 days prior to ship observations. Daily SST (Table 1) collocated with the cruise track was used in modeling historical temperature. Salinity was assumed to remain constant, equal to the salinity measured at cruise sampling, while vertical mixing was ignored in these calculations due to lack of subsurface gas saturation data. Sea ice concentration (Table 1) collocated with the cruise track was used in adjusting air-sea gas exchange with a linear scaling of both the $O_2$ piston velocity and diffusive gas exchange based on the fraction of sea ice coverage, while bubble flux was assumed to be negligible when sea ice was present. The bubble scaling coefficient, β, was set to 0.5 for these calculations. This value was found to be optimal for the Izett and Tortell (2021) dataset, and sensitivity tests were conducted with this dataset that indicated our modeling results did not depend strongly on β.

## 3. Results and discussion

### 3.1. Spatial patterns

A comparison of spatial distributions of $\Delta O_2$ with $\Delta O_2/Ar$ for OS1901 illustrates how oxygen supersaturation and net biological oxygen supersaturation are related (Fig. 1). Note that there are regions (e.g., red circle at 60°N) with strong oxygen supersaturation that were co-located with negative $\Delta O_2/Ar$, suggesting that oxygen supersaturation was purely driven by physical factors (e.g., wind and bubbles or warming). The biological signal opposed this trend, but did not completely compensate for physical effects. In other areas, $\Delta O_2$ was greater than $\Delta O_2/Ar$, suggesting a mix of physical and biological forcing of oxygen supersaturation. The spatial patterns in $\Delta O_2/Ar$ indicated areas of large net biological supersaturation with $\Delta O_2/Ar$ peaks above 30% near the Aleutian arc, in Chirikov Basin and southwest of Point Hope. Regions in Chirikov Basin and southwest of Point Hope are established biological hotspots (Grebmeier et al., 2015).

In these biological hotspots, elevated underway chlorophyll-a (from a Seabird ECO-FL fluorometer) corresponded with high $\Delta O_2/Ar$ on 3 out of 4 instances (Fig. 2). The peak in $\Delta O_2/Ar$ that did not correspond to elevated fluorescence occurred in the region off Point Hope, which was occupied twice (August 11th and August 23rd). While low concentrations of chlorophyll-a were observed during the first occupation, a chlorophyll peak was observed on the later occupation. A mismatch between chlorophyll-a and $O_2/Ar$ is expected at times because of the different residence timescales associated with dissolved gases and chlorophyll production in the surface ocean: the $O_2$ signal from a bloom will take 2–3 weeks to reequilibrate with the atmosphere, whereas chlorophyll biomass can sink or be consumed by grazers over shorter timescales. Chlorophyll-a data (Table 1) from MODIS-Aqua (NASA Goddard Space Flight Group et al., 2018) were sparse in the weeks prior to shipboard measurements, but the edge of a bloom with elevated chlorophyll-a was seen off of Point Hope on August 4, 2019, about 7 days prior to shipboard measurements in the same location (not shown). This elevated biological production was indicated in the shipboard $O_2/Ar$, while the production of chlorophyll-a may have attenuated over a shorter timescale, resulting in low underway fluorescence. In addition, fluorescence can be impacted by photochemical quenching, which can cause fluorescence to diverge from chlorophyll concentrations (the chlorophyll shown in Fig. 2 was calculated directly from fluorescence using manufacturer-supplied coefficients) (Zankel et al., 1968). Photochemical quenching could have contributed to the low estimate of chlorophyll on August 11, which was sampled in late afternoon, yet the quenching effect is not expected to fully deplete the detection of chlorophyll observed on this date.

In the Bering Sea, there are several regions where $\Delta O_2$ is positive and $\Delta O_2/Ar$ is negative (Fig. 1), consistent with physical supersaturation of oxygen in the surface ocean due to both warming water and increased wind speed ($\Delta O_2 > 0$) and net heterotrophic biological activity ($\Delta O_2/Ar < 0$). This hypothesis is supported by both high frequency winds and recent warming (Fig. 3, panels C and D), where this region of the Bering Sea corresponds to August 4–5. In Chirikov Basin, $\Delta O_2/Ar$ was variable, with patches of large supersaturation as well as undersaturation that could be attributed to the dynamic nature of water masses mixing in this area (Danielson et al., 2017). The areas with both negative and positive

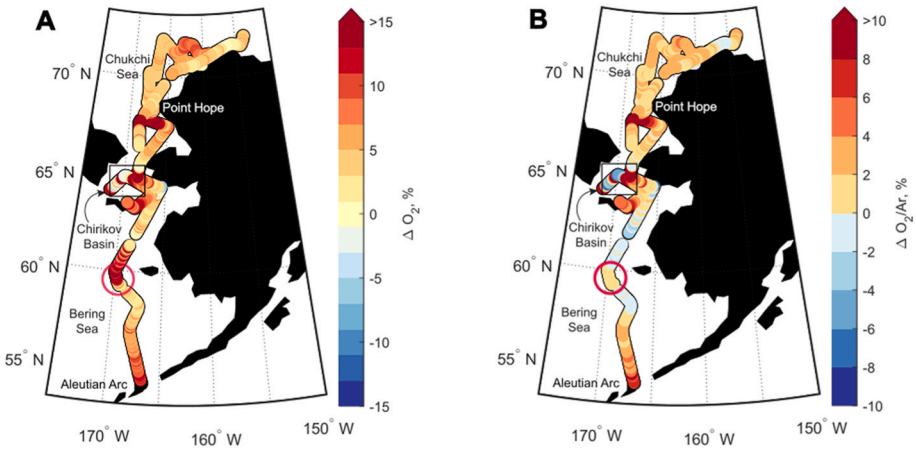


**Fig. 1.** $\Delta O_2$ and $\Delta O_2/Ar$ along the cruise track (scale attenuated to emphasize near-equilibrium trends, note different scales in A and B). These trends in $\Delta O_2/Ar$ are also seen in $\Delta O_2/N_2$ (not shown), with additional noise. The cruise began in Dutch Harbor, AK and ended in Nome, AK. Breaks in the track line were due to gaps in data collection.

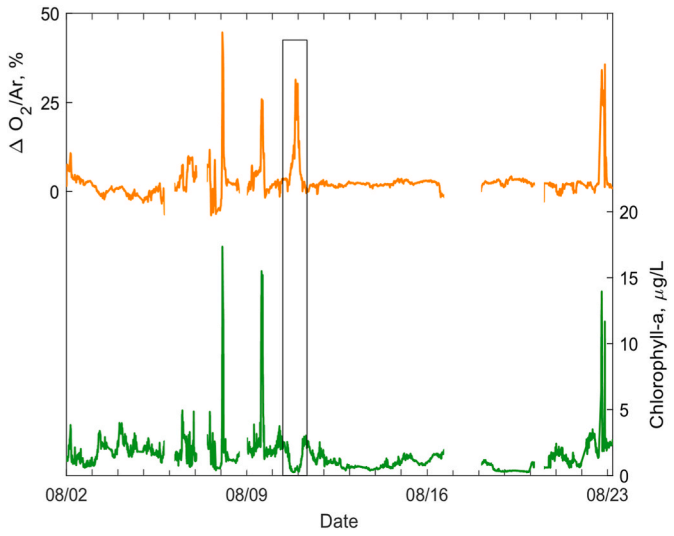


**Fig. 2.** Underway measurements of $\Delta O_2/Ar$ and chlorophyll-a based on fluorescence throughout the cruise. Boxed area indicates occupation off of Pt. Hope with low chlorophyll and elevated $\Delta O_2/Ar$.

$\Delta O_2/Ar$ in the western part of Chirikov Basin are in significantly colder, saltier, nitrate-rich water (salinity >32.5, $NO_3$ > 20 μM from an underway nutrient sensor, data not shown) typical of Anadyr water (Grebmeier et al., 2006). The $\Delta O_2/Ar$ signals here likely reflect a combination of recent vertical mixing of subsurface water with a depleted $O_2$ signature to the surface and patchy production sparked by high nutrient Anadyr water when light and stratification conditions were favorable. In the majority of the Chukchi Sea, net biological oxygen supersaturation was positive, indicating net autotrophy (median $\Delta O_2/Ar = 2\% \pm 2.1\%$, median absolute deviation = 0.8% when excluding biological hotspots where $\Delta O_2/Ar > 5\%$).

### 3.2. EIMS-GTD comparison

There was relative agreement between $\Delta O_2/N_2$ and $\Delta O_2/Ar$ for OS 1901, with both ratios indicating net biological oxygen supersaturation for the majority of the cruise (Fig. 3A). Throughout the cruise, $\Delta O_2/N_2$ was slightly less than $\Delta O_2/Ar$, yet in areas of large biological oxygen supersaturation, the ratios were observed to differ, where $\Delta O_2/N_2$ was consistently greater than $\Delta O_2/Ar$ (Fig. 3A). The response time associated with the EIMS equilibrator cartridge effectively slows down the $\Delta O_2/Ar$ measurements, resulting in $\Delta O_2/Ar$ that did not reach the true maximum value during sharp gradients, while $\Delta O_2/N_2$ is likely capturing these maxima more accurately due to the faster response time. This is supported by discrete $O_2/Ar$ bottle samples, which were greater than corresponding EIMS $O_2/Ar$ measurements by about 5% during two steep gradients on this cruise, corroborating the idea that the EIMS is not measuring the true value during these peaks in net biological oxygen production.

The median of diff-Δ over the cruise was 0.53%, indicating that $\Delta O_2/Ar$ was generally greater than $\Delta O_2/N_2$, while there were many large excursions from these values (Fig. 3B). In particular, deviations in diff-Δ occurred during time periods where strong gradients in oxygen were encountered and in areas with overwhelming bubble influence (shaded regions, Fig. 3B). The spread of diff-Δ remains similar when observing all diff-Δ values compared to baseline values (which excludes data associated with steep gas peaks and data with substantial bubble noise, Fig. 4), with a roughly normal distribution of diff-Δ where 90% of baseline observations were between −2.2% and 3.5%.

While the median value of diff-Δ was small overall (0.53%) and is comparable to the uncertainty in $O_2/N_2$ (as discussed in section 3.6), it is still useful to understand potential biases that may contribute to differences between $O_2/Ar$ and $O_2/N_2$ for this data. A potential source of bias in $\Delta O_2/N_2$ and thus diff-Δ may arise from the assumed saturation of less prevalent gases, particularly Ar. On this cruise, Ar concentrations were determined by EIMS $O_2/Ar$ ratio and optode oxygen measurements (where $[Ar] = [O_2]_{optode}/[O_2/Ar]_{EIMS}$), yet these values were not used in calculations of $\Delta O_2/N_2$, as this study is intended to simulate the comparability of these methods, and the inclusion of calculated Ar values is not anticipated to be available with most GTD deployments. If these calculated values for Ar were included, which indicate Ar was consistently supersaturated throughout this cruise, the bias in diff-Δ does not change considerably, with a median of 0.48%. We investigate other potential sources of bias from physical forcing in section 3.3.

### 3.3. Evaluating physically-driven bias in $O_2/N_2$ relative to $O_2/Ar$

Differences in $\Delta O_2/Ar$ and $\Delta O_2/N_2$, i.e., diff-Δ, are expected due to a variety of physical factors including gas solubility, bubble injection, and gas exclusion principles. For example, an increase in temperature instantaneously changes the gas solubility in the water mass; the solubility of Ar and $O_2$ will change similarly due to their comparable solubility, while $N_2$ solubility decreases to a lesser extent because it is less soluble. This difference in temperature effect between $N_2$ and Ar appears small in the individual gas saturation anomalies (Fig. 5A) but becomes amplified when calculating gas ratios due to the dissimilarity between

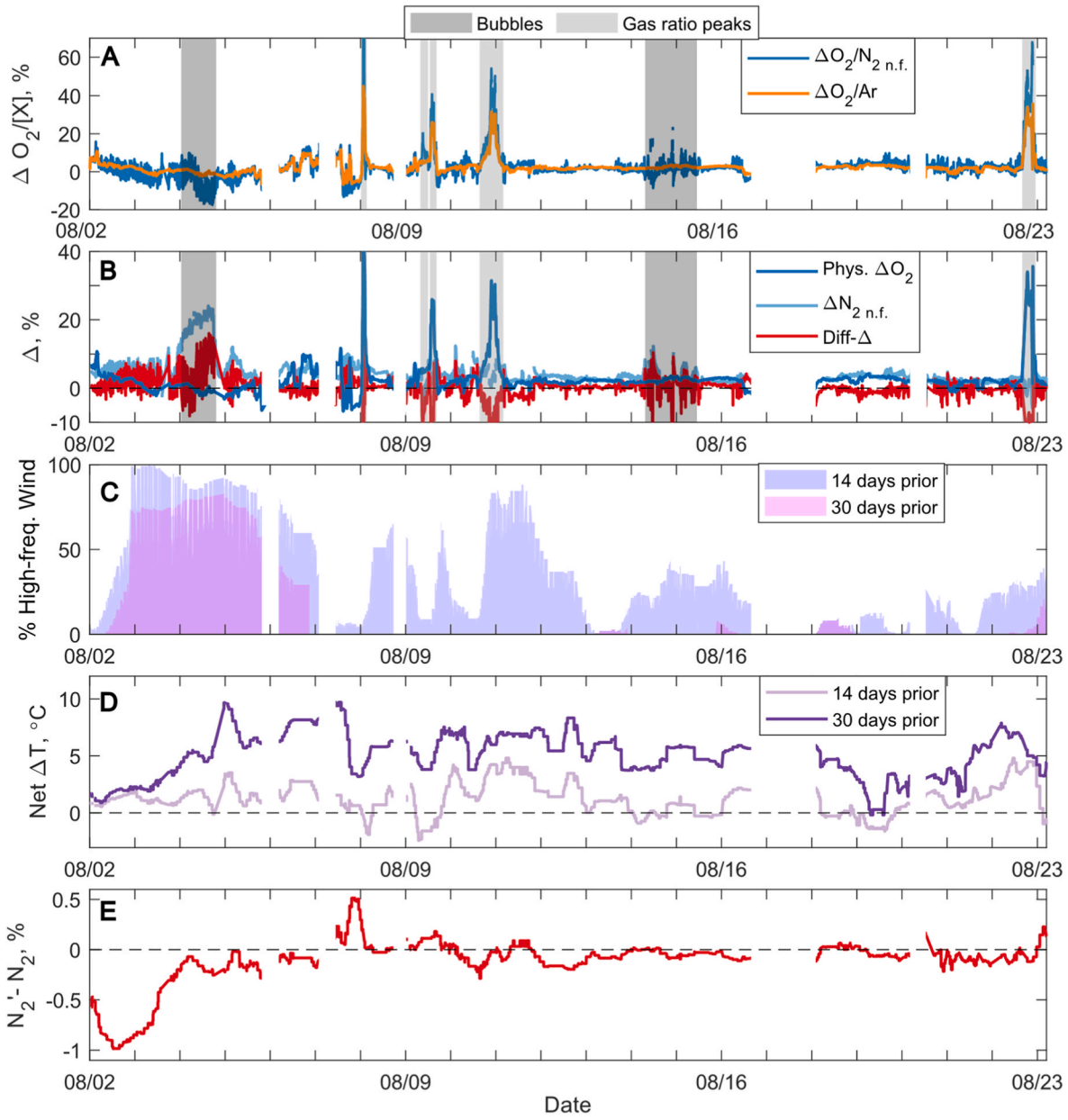


**Fig. 3.** (A) Time-series of $\Delta O_2/Ar$ and noise-filtered (n.f.) $\Delta O_2/N_2$, where shaded areas indicate either noise due to bubbles in the underway seawater line or large gradients in gas ratios as determined by observation. The $\Delta O_2/N_2$ peak off the chart is at 119%. (B) Time-series of Diff-Δ, $\Delta O_2$-physical, and noise-filtered $\Delta N_2$, where artifacts of the data due to mismatched gas ratio peaks (Diff-Δ shaded in light gray) are off the chart and should not be considered. (C) Percent of 3-hourly average wind speed measurements exceeding 10 m $s^{-1}$ over 14 and 30 days prior to sampling where collocated with cruise track. (D) Net temperature change over 14 and 30 days prior to sampling, collocated with cruise track, based on satellite SST reanalysis. (E) Difference between $N_2$' and $N_2$ along the cruise track.

$N_2$ and $O_2$. The result is an $\Delta O_2/N_2$ ratio change in response to temperature that is 12 times greater than $\Delta O_2/Ar$ (Fig. 5B). For example, warming of 5°C would result in relatively similar increases in $O_2$, $N_2$, and Ar saturations (11.3%, 10.4%, and 11.2% respectively) but pronounced differences between the $\Delta O_2/Ar$ and $\Delta O_2/N_2$ gas ratios (0.18% and 0.83% respectively). The resulting change in diff-Δ ($\Delta O_2/Ar$ - $\Delta O_2/N_2$) would be −0.65%. This warming-induced saturation signal will erode via exchange with the atmosphere over subsequent weeks as the upper ocean re-equilibrates to the new temperature (Fig. 6A).

Conversely, wind-driven bubble injection creates a gas supersaturation due to enhanced gas injection which increases over the period of enhanced wind. Bubble injection and bubble exchange, parameterized as wind-driven based on the equations of Woolf and Thorpe (1991), will increase individual gas saturations but will decrease the $\Delta O_2/N_2$ ratio due to the high mole fraction of $N_2$ in the atmosphere and the relatively low solubility of $N_2$ in seawater. The wind-driven supersaturation of $N_2$ is much larger than the supersaturation of more soluble gases ($O_2$, Ar), such that enhanced wind will increase diff-Δ. If wind speed increases from 5 m $s^{-1}$ to 15 m $s^{-1}$ and remains at 15 m $s^{-1}$, the resulting equilibrium diff-Δ will reach a maximum of 1.8%, where diff-Δ will equal 95% of the maximum (1.8%) in 2 days based on the estimated effect of bubbles injected into the surface ocean and the solubility differences between $N_2$ and Ar (Fig. 6B). The expected change in gas saturation and gas ratio saturation from temperature change and enhanced wind are indicated in Fig. 6 where the relaxation back to equilibrium (defined as within 10% of the equilibrium value) following either a high wind event or temperature change is slow (~6–8 weeks).

Because $O_2/N_2$ is likely to be more sensitive to physical forcing than $O_2/Ar$, one way of assessing causes of observed diff-Δ and hence biases in $O_2/N_2$ is by comparing diff-Δ values to an approximation of physical

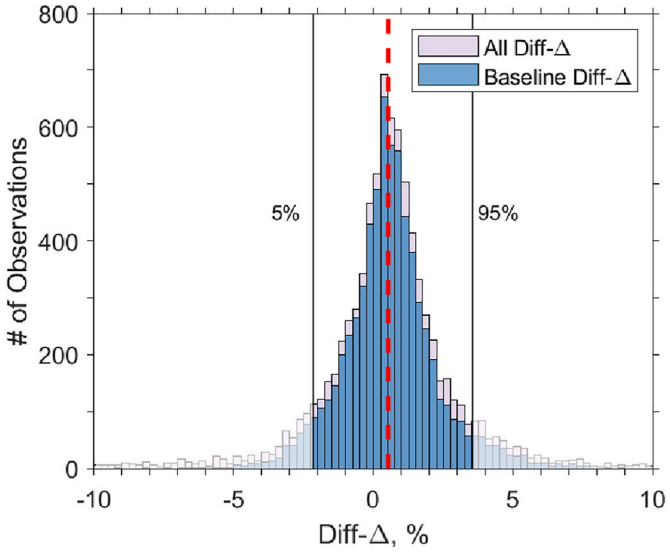


**Fig. 4.** Histogram of diff-Δ observations with all values and with baseline values (when erroneous data due to bubbles and steep gas peaks are excluded).

forcing, estimated as:

$$\Delta O_2^{phys} = \Delta O_2^{total} - \frac{[Ar]}{[Ar]_{sat}}\Delta(O_2 / Ar). \quad (11)$$

where the last term represents $\Delta O_2^{bio}$ (Eveleth et al., 2017). When $\Delta O_2^{phys}$ is positive, a positive physical supersaturation of oxygen is estimated and could be indicative of recent warming of the water mass or potential influence of bubbles. Along the same lines, a negative value is expected when biological oxygen saturation is greater than total oxygen saturation, potentially caused by recent cooling. Argon was observed to be supersaturated for a majority of this cruise, such that $\Delta O_2^{phys}$ had a mean value of 2.6% in this cruise (Fig. 3B). This $\Delta O_2^{phys}$ estimate may indicate that the small difference between $O_2/Ar$ and $O_2/N_2$ is due to recent wind-forcing on the water mass; this is because of a combination of the physical oxygen supersaturation and median positive diff-Δ, where positive diff-Δ results from bubbles or cooling (and negative diff-Δ results from warming). Physical forcing estimates from this cruise (Fig. 3C and D) did not appear to be directly related to observed diff-Δ over the span of this cruise, yet a more accurate approach of modeling water mass history would better approximate the solubility-based differences between $O_2/Ar$ and $O_2/N_2$.

Recently, Izett and Tortell (2020) introduced a calculated value, $N_2$', that corrects for solubility differences between $N_2$ and Ar using historical water mass data, where $N_2$' is an approximation of Ar, a physical analogue to $O_2$ (Izett and Tortell, 2020b; Izett et al., 2021). If $N_2$' and $N_2$ differ significantly, a large component of physical bias exists in $O_2/N_2$ due to physical forcing and reequilibration dynamics, but $O_2/N_2$' could be calculated to adjust for the expected solubility differences due to the historical physical forcing. Our estimated $N_2$' is similar to measured $N_2$ for most of this cruise (Fig. 3E), with deviations that may be attributed to wind and temperature change (Fig. 7).

Over the first two days of the cruise in the southern Bering Sea, wind was the predominant driver of the negative difference between $N_2$' and $N_2$, which was also the case intermittently over the following few days (Fig. 7A). This was determined based on both the relatively high-frequency winds, small temperature change (Fig. 3), and the results of a pair of $N_2$' modeling calculations in which either historical temperature or wind speed was held constant at values measured on the cruise (Fig. 7). After the initial wind-dominated days in the Bering Sea, the combination of wind and warming temperatures resulted in near-zero difference in $N_2$' and $N_2$, where the two factors likely balanced each other out at times. The estimates of $N_2$' contributions do not combine to

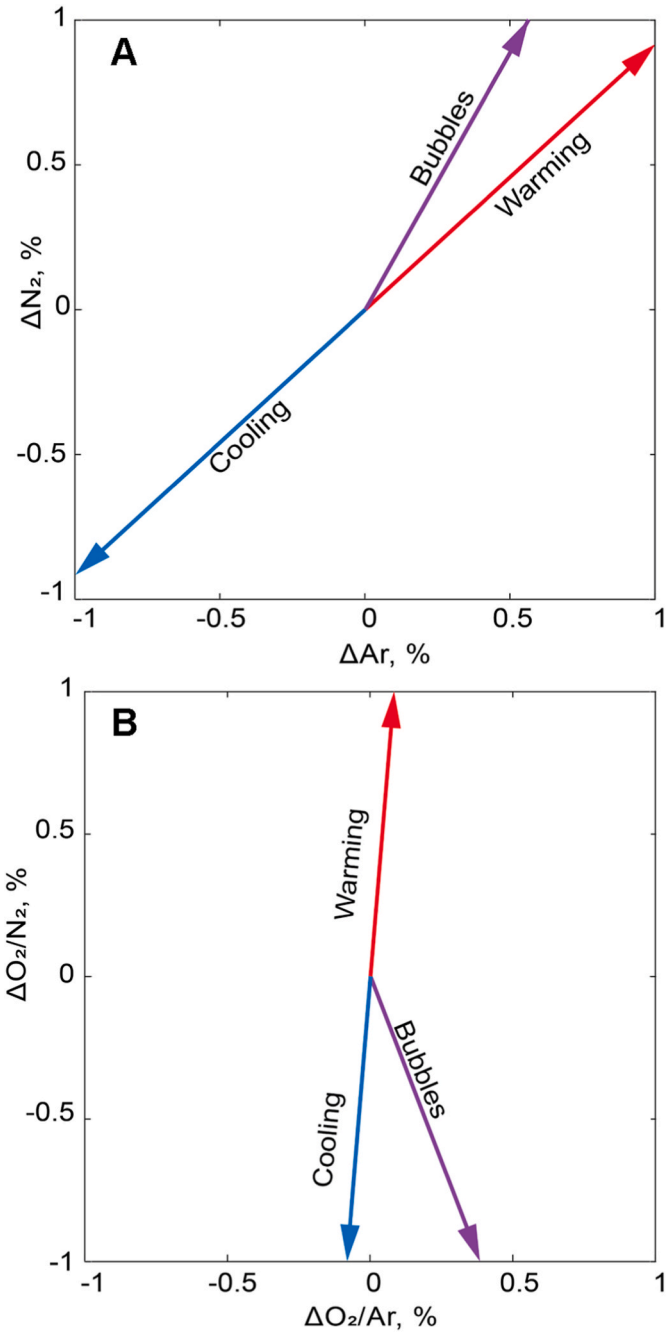


**Fig. 5.** Expected changes in ΔAr, $\Delta N_2$, $\Delta O_2/Ar$ and $\Delta O_2/N_2$ due to temperature change and bubble injection. Baseline parameters include salinity of 32 and starting temperature of 10°C, where temperature changes linearly for warming and cooling and wind speed increases linearly to represent the effect of bubbles.

equal the calculated difference in $N_2$' and $N_2$, as assumptions were made about the constant temperature or wind speed that contribute to erroneous estimates, yet they are a rough approximation of the role each factor plays in the correction of solubility differences.

The difference in $N_2$' and $N_2$ throughout the cruise was not directly correlated to the estimates of physical forcing described here (high-frequency wind, average wind speed, and net temperature change over 14 and 30 days, Fig. 3). This is suspected to be in part due to the cumulative nature of physical forcing by temperature change and wind, inaccuracies in satellite-based wind speeds, and the averaging that was used in these estimates, where wind and temperature changes in the day or two prior to measurement will be more strongly reflected in $N_2$' than

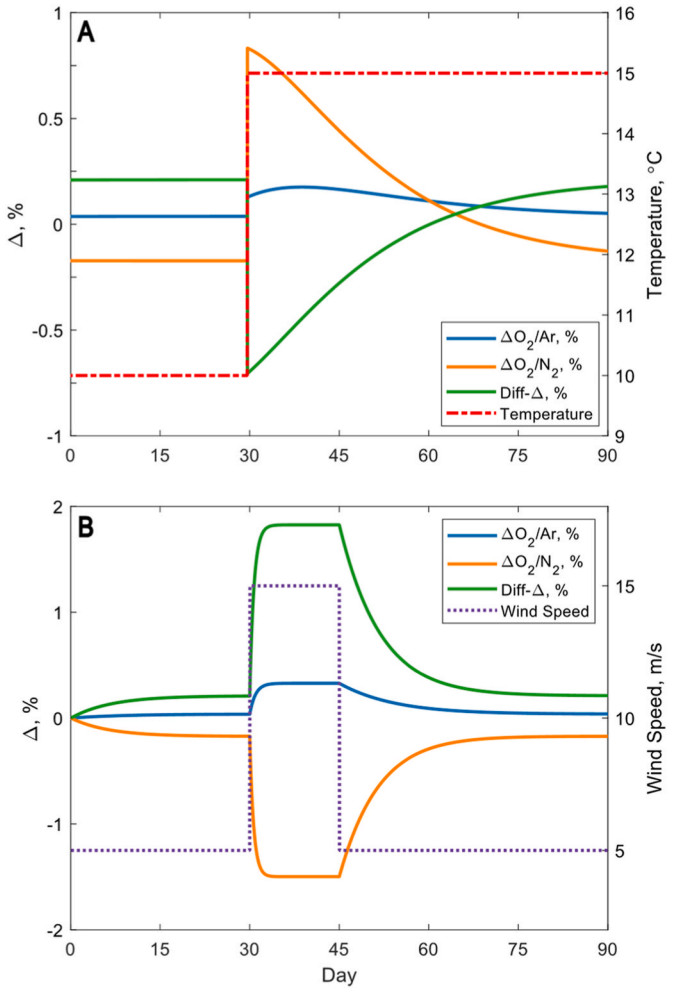


**Fig. 6.** Box model of gas saturation change in $\Delta O_2/Ar$ and $\Delta O_2/N_2$ with (A) warming water and (B) increased wind speed. Baseline parameters include a mixed layer depth of 20 m, temperature of 10°C, salinity of 32 and wind speed of 5 m $s^{-1}$.

those two weeks prior. Additionally, the calculations of $N_2$' performed here excluded vertical mixing due to lack of gas saturation data at depth, yet complete absence of vertical mixing is unlikely and therefore contributes to uncertainty in estimated $N_2$'.

The small overall differences in $N_2$' and $N_2$ throughout most of this cruise were consistent with findings by Izett et al. (2021) of minimal difference in these tracers in the Canadian Arctic Archipelago and Baffin Bay. This suggests that application of the $O_2/N_2$ approach could be promising in the Pacific Arctic region, but further evaluation under a range of physical conditions is still needed. The use of $O_2/N_2$' could improve the utility of the GTD method, yet the advective nature of water masses should be accounted for in a study area, where highly advective regions may be inaccurately modeled by georeferenced data prior to sampling. In this study region, where advection of water masses can be relatively rapid, the reconstructed water mass history used in calculating $N_2$' could be erroneous at times.

### 3.4. Sea ice and biological influences on dissolved $O_2$, $N_2$, and Ar

Other factors that influence gas saturation include sea ice formation, sea ice melt, and biologically-driven $N_2$ fixation or denitrification. For this dataset, we expect these processes to contribute insignificantly toward driving differences between $O_2/N_2$ and $O_2/Ar$. During sea ice formation, brine rejected from the ice matrix is expected to be enriched in Ar, $O_2$, and $N_2$ due to the exclusion of larger gas molecules during the freezing process. This brine sinks to depth, enriching deep water in these gases. When vertical mixing of these deep waters occurs, a brine signal may be observed in the resulting water, which is expected to be enriched in Ar compared to $N_2$ based on gas partitioning between bubbles, ice, brine, and residual water (Hood 1998; Hood et al., 1998). In contrast, the meltwater signal is expected to be depleted in larger gases (Ar, $O_2$, $N_2$) due to gas exclusion during sea ice formation. This meltwater effect is not anticipated to be represented in this dataset due to lack of sea ice during and directly prior to this cruise, but brine signatures could be observed in areas where vertical mixing brings waters that have been seasonally isolated at depth to the surface.

Biological influences on dissolved $N_2$ in the ocean, including nitrogen fixation and denitrification, typically have a small overall effect on the dissolved $N_2$ saturation anomaly ($\Delta N_2$). The effect of nitrogen fixation, calculated based on the maximum rate of nitrogen fixation estimated by Shiozaki et al. (2018) in the Chukchi Sea, is negligible on $\Delta N_2$ (<0.01%). The effect of denitrification on the shallow Bering and Chukchi shelves has a potentially greater effect on $N_2$. Vertical mixing of deep water containing biologically elevated dissolved $N_2$ will influence the $O_2/N_2$ ratios measured at the surface, resulting in lower-than-expected $\Delta O_2/N_2$. With seasonal dissolved inorganic nutrient deficits (3.9 μM N) at depth on the Chukchi shelf (Mordy et al., 2021), vertical mixing of 20% of the water column would result in a 0.06% decrease in $\Delta O_2/N_2$ in the surface mixed layer, a small and likely indiscernible bias. Since the Chukchi Sea is seasonally well-stratified, more significant vertical mixing of the water column is only likely to occur near coastal features or areas with enhanced mixing, such as near Bering Strait.

### 3.5. Net community production

The median NCP estimated by $O_2/Ar$ and $O_2/N_2$ was 9.3 ± 2.8 and 7.9 ± 3.2 mmol $O_2$ $m^{-2}$ $day^{-1}$, respectively, for all regions with comparable data (which excludes bubble-impacted areas, as well as one region in Chirikov Basin with a clear vertical mixing signal). The overall NCP estimated by $O_2/Ar$ and $O_2/N_2$ are similar, with slightly larger values based on $O_2/N_2$, while differences include the discrepancy in maximum NCP in regions with large gradients as previously discussed, as well as increased noise in $O_2/N_2$ signal (Fig. 8).

The median NCP based on $O_2/Ar$ measurements was 9.8 mmol $O_2$ $m^{-2}$ $day^{-1}$, while 95% of the values fell between −18 and 100 mmol $O_2$ $m^{-2}$ $day^{-1}$. Assuming NCP is primarily new production fueled by nitrate, we use an $O_2$:C ratio of 1.4 (Laws 1991), where $O_2/Ar$-based NCP ranged from below zero to >1000 mg C $m^{-2}$ $day^{-1}$, with a median of 84 mg C $m^{-2}$ $day^{-1}$ during this August cruise. Since this measurement technique integrates over the preceding weeks, this unique dataset may better capture episodic events that are missed by shorter-term incubations. These measurements therefore fill an important temporal gap between short-term incubations and large-scale seasonal drawdown estimates calculated at the regional scale. By utilizing $O_2/N_2$-based NCP estimates in remote regions including the subpolar and polar seas, variability due to seasonal patterns and episodic events contributing to NCP could be more completely understood.

Given that these NCP estimates fill a unique temporal gap it is useful to compare to prior estimates. Seasonal NCP estimates based on DIC and nutrient drawdown (Mathis et al., 2009; Codispoti et al., 2013) in the Chukchi Sea include the spring bloom, and are therefore expected to be considerably higher than our rates measured in August, post-bloom. Annual measurements (Mordy et al., 2020) include the dark, ice-covered winter when production is absent and may be more in line with our post-bloom estimates. Generally, these patterns are what we see when we compare to prior estimates (Table 2). However, it is important to note that interannual variability in this region is large, and the Chukchi and Bering Seas were noted to have particularly high sea surface temperatures in 2019, which may have led to an uncharacteristic environment (Andersen et al., 2020).

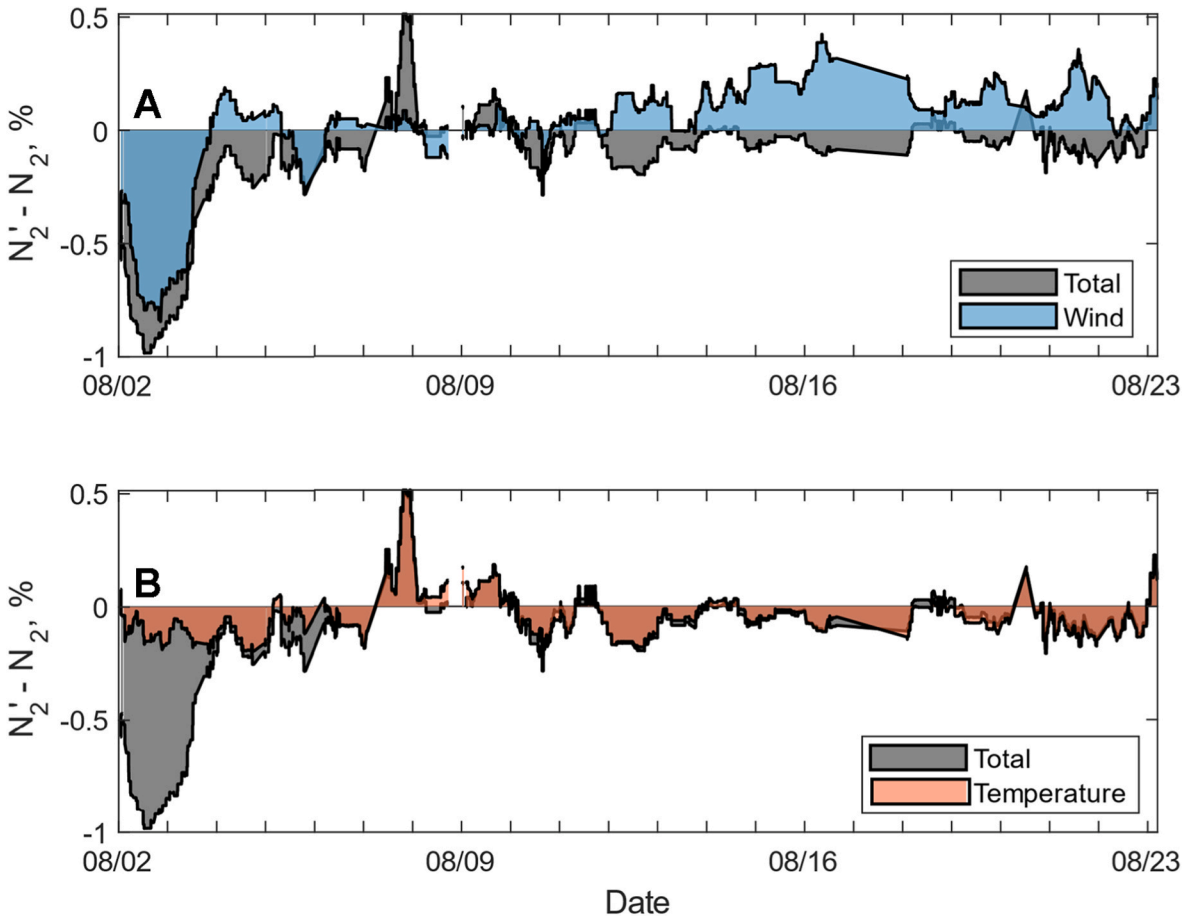


**Fig. 7.** (A) Modeled $N_2$' – $N_2$ compared to the wind component, $N_2'_{wind}$ – $N_2$. $N_2'_{wind}$ is estimated by taking the difference between $N_2$' and $N_2$' when historical wind speed is set constant, equal to wind speed at cruise occupation. Areas where these align indicate that historical wind speed is the main driver of saturation differences. (B) Modeled $N_2$' – $N_2$ compared to the temperature component, $N_2'_{temp}$ – $N_2$. $N_2'_{temp}$ is estimated by taking the difference between $N_2$' and $N_2$' when historical sea surface temperature is set constant, equal to temperature at cruise occupation. Areas where these are similar indicate that past temperature change is the main driver of saturation differences.

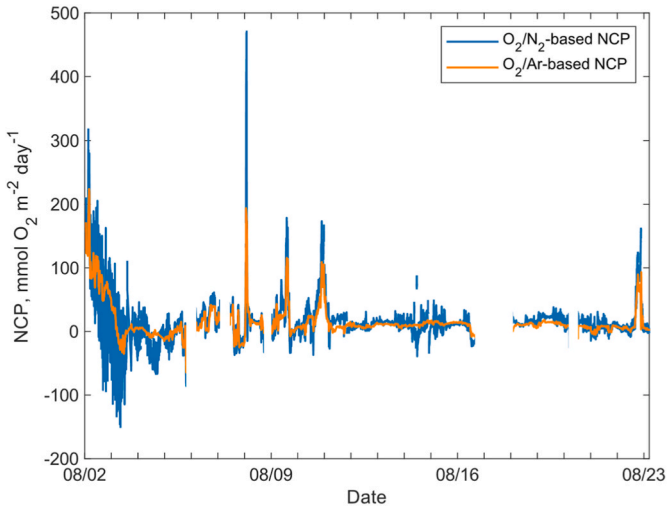


**Fig. 8.** NCP calculated based on $O_2$/Ar and residual filtered $O_2/N_2$ for measurements within the bounds described.

With the spatially resolved data from this cruise, patterns of surface productivity can be assessed, and potential drivers of biological production can be explored. Areas of high NCP from this cruise were consistent with previously observed biological hotspots in the Chirikov Basin and off of Point Hope (Distributed Biological Observatory regions 2 and 3, respectively, Grebmeier et al., 2010). More broadly, the observations illustrate that NCP is spatially patchy, as has been previously noted (Juranek et al., 2019). These patterns may be missed by traditional incubation sampling approaches. Patchy regions of high NCP on this cruise may be a result of nutrient input through the convergence of water masses, which was noted in Chirikov Basin where Anadyr water was present, as well as near Pt. Hope due to the combination of upstream mixing in Bering Strait and water flow around the headland of Pt. Hope (Fig. 9). In the Chirikov Basin, NCP calculations were determined to not meet steady-state requirements, since this area was subject to significant mixing as noted by CTD casts with uniform temperature and salinity profiles. In the Pt. Hope region, the high NCP observed by gas ratio methods, which at times contrasted with the measured chlorophyll, was indicative of the intermittent nature of blooms in this region. These variations are due to the coexistence of favorable light and nutrient conditions, which can vary due to changes in water masses, mixed layer depth, and/or wind patterns.

In the southern Bering Sea, NCP was elevated near the Aleutian Islands and near Bering Strait, while lower values were estimated in the eastern central Bering Sea where high winds were observed. The southern Bering Sea had some of the highest NCP measurements with a bimodal distribution where the majority of NCP estimates were near equilibrium and a smaller grouping of values were between 50 and 100 mmol $O_2$ $m^{-2}$ $day^{-1}$. The northern Bering Sea also had a large proportion of NCP estimates near equilibrium, with some elevated values

**Table 2**
NCP comparisons in Chukchi Sea.

| Method | NCP (mg C $m^{-2}$ $day^{-1}$) | Region | Timescale | Source |
|---|---|---|---|---|
| DIC Drawdown | 8 to >2000 (range of values) | Northeast Chukchi Sea | Seasonal, spring to summer, integrated over upper 30 m | Mathis et al. (2009) |
| Nutrient drawdown | 1167 | Southern Chukchi Sea | 60-day growing period, integration depth chosen based on maximum nutrient drawdown | Codispoti et al. (2013) |
| Seasonal nitrate | 82 to 192 | Eastern Chukchi Sea | Annual, between 2010 and 2018 | Mordy et al. (2020) |
| Shipboard $O_2$/Ar | 8 to 86 [1–10 mmol $O_2$ $m^{-2}$ $day^{-1}$] | Chukchi Sea | Integrated over few weeks in October 2011 and 2012 | Juranek et al. (2019) |
| Shipboard $O_2$/Ar | 84 [9.8 mmol $O_2$ $m^{-2}$ $day^{-1}$] | Chukchi Sea | Integrated over few weeks in August 2019 | this study |

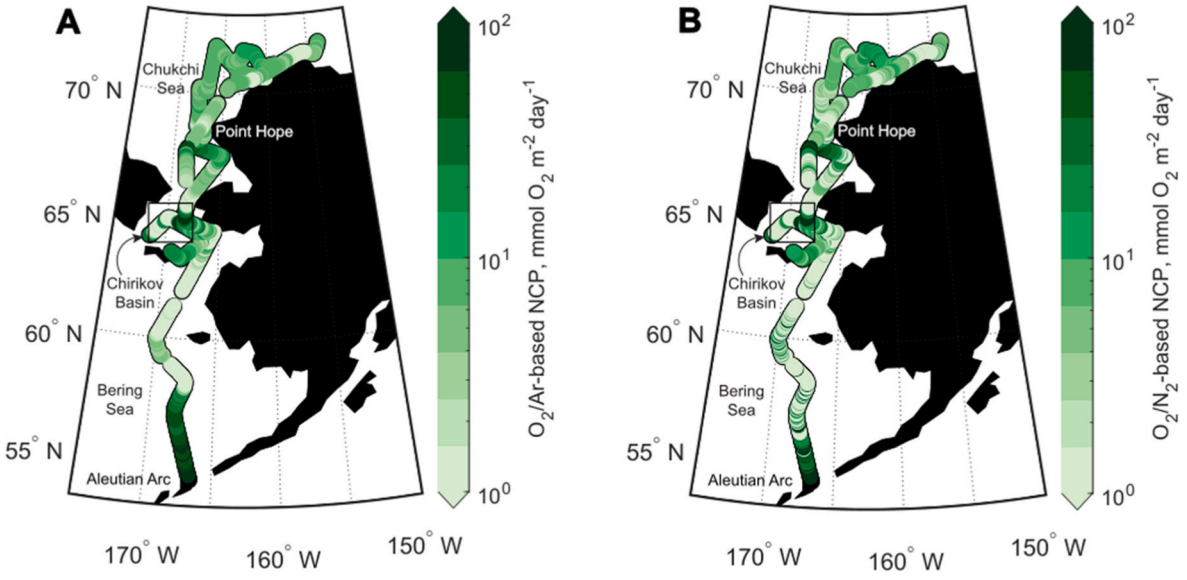


**Fig. 9.** (A) $O_2$/Ar-based NCP and (B) $O_2$/$N_2$-based NCP along the cruise track (scale attenuated, where range is −64 to 224 and -184 to 491, respectively).

primarily around Chirikov Basin and Bering Strait. The most dynamic region observed on this cruise was the southern Chukchi Sea, where NCP was generally positive with an average of 24 mmol $O_2$ $m^{-2}$ $day^{-1}$, while this was also the region where hotspots were observed near Pt. Hope. The northern Chukchi and Beaufort seas had relatively consistent NCP that was representative of the median NCP throughout the cruise of near 10 mmol $O_2$ $m^{-2}$ $day^{-1}$, with limited variance in these areas.

By observing the seasonal patterns in NCP in high resolution, connections to wind events and water mass convergences could be better understood, ultimately providing a better foundation for deciphering future patterns of productivity within this dynamic environment. As this cruise took place in an unusually warm year with early ice retreat, these observations from August 2019 may deviate from patterns observed in colder years.

### 3.6. Uncertainty analysis

To estimate uncertainty in EIMS- and GTD-based NCP, we used a Monte Carlo approach that involves randomly varying the estimated error of each parameter involved in calculating NCP, assuming a normal distribution of error. The values used in these determinations are found in Table 2, where uncertainty was calculated based on 1000 determinations of $\Delta O_2$/Ar- and $\Delta O_2/N_2$-based NCP with Eq. (10) for gas ratios observed on this cruise. Absolute uncertainty in the measurement of $O_2$/Ar of ±0.25% was determined by the standard deviation of $O_2$/Ar in air standards (n = 27) measured by IRMS, since EIMS $O_2$/Ar measurements were corrected to the calibration bottle samples analyzed by IRMS. For GTD-based measurements, an absolute precision in the measurement and calculation of $O_2/N_2$ of ±0.57% was determined by propagation of error in Eqs. (6) and (7) (Table 3). Izett et al. (2021) estimated the uncertainty in $\Delta O_2/N_2$ at 1.3%, which also included uncertainties for warming-induced supersaturation in the underway ship lines, calibration of $O_2/N_2$, and the assumptions in constraining Ar. This error analysis may better approximate the uncertainties in $\Delta O_2/N_2$, yet the effect of this random uncertainty on NCP estimates is very small due to the far greater uncertainty in constraining the gas transfer term.

**Table 3**
Error estimates used in Monte Carlo approach of uncertainty and output uncertainty in $\Delta O_2$/Ar and $\Delta O_2/N_2$.

| Source | Estimated Error | |
|---|---|---|
| $O_2/Ar_{meas}$ | 0.25% (St. Dev. Of $O_2$/Ar in air) | |
| $O_{2sol}$ | 0.3% (Garcia and Gordon 1992) | |
| Gas exchange, k | 20% (Wanninkhof 2014) | |
| GTD total pressure | 0.2% or 2 mbar (Pro-Oceanus TDGP manual) | |
| $O_2$ (Winkler-corrected optode) | 0.5% or 1.1 mbar (McNeil et al., 2005) | |
| Atmospheric pressure (NCEP reanalysis) | 0.5% or 5 mbar (Padin et al., 2007) | |
| Uncertainty | Absolute | Relative error, $\Delta O_2$/[X] = 1% or 10% |
| $O_2$/Ar | 0.25% | 1 ± 0.41% 10 ± 0.42% |
| $O_2/N_2$ | 0.57% | 1 ± 0.66% 10 ± 0.75% |

Uncertainty in the gas transfer coefficient, $k_{O2}$ (±20%) (Wanninkhof 2014), makes up the largest component of uncertainty in NCP. The resulting uncertainty for a simulated NCP of 10 mmol $O_2$ per $m^2$-day from $O_2$/Ar and $O_2/N_2$ is 30% and 36%, respectively, with a proportionally lower error with larger NCP rate. The uncertainty in $O_2$/Ar-based NCP ranged from 16% to >100%, while the uncertainty for

$O_2/N_2$-based NCP ranged from 20% to >100%. Importantly, while uncertainty in $\Delta O_2/N_2$ becomes large in areas where net biological oxygen supersaturation nears zero, these estimates still discern the relative magnitude and direction of NCP for the majority of observations on this cruise, so long as the oxygen measurements used to compute $O_2/N_2$ are well-calibrated.

The uncertainty outlined above is based on the accuracy in the measurement and calculation of $\Delta O_2/N_2$, and does not include potential biases from physical forcing that cause this tracer to inaccurately track $\Delta O_{2bio}$ (see Section 3.3). When comparing median diff-Δ (0.53%) to the methodological uncertainty of 0.57% in $\Delta O_2/N_2$, the bias represented by diff-Δ is of similar magnitude. The distribution of baseline diff-Δ, between −2.2% and 3.5% for 90% of observations, is attributed to the cumulative saturation effects of both bubbles and temperature change, while potential variations in Ar saturation could have also played a small role. Bubbles were the primary driver in the southern Bering Sea, while temperature change was likely more important in the Chukchi Sea, as inferred from the modeling described above.

### 3.7. Strengths and weaknesses of GTD and EIMS approaches

A potential limitation of gas ratio estimates from a GTD is the dependence on accurate oxygen measurements when calculating $O_2/N_2$. This requires optode calibration to adjust for offsets and drift, where a 5% inaccuracy in measured optode $O_2$ (the average offset on this cruise), would result in a difference of 6.5% in $O_2/N_2$. Without reliable oxygen calibrations, this scale of difference could result in ambiguous NCP estimates derived from $O_2/N_2$, although areas with strong biological signals are still qualitatively identified despite this potential uncertainty. This is expected to be a greater issue when frequent $O_2$ calibration samples are not feasible, e.g. with autonomous deployments, although periodic air calibration of deployed oxygen sensors could serve as an alternative calibration method (Bittig and Körtzinger 2015; Bushinsky et al., 2016).

A challenge experienced with the GTD-optode system on this cruise was the effect of bubbles in the surface ocean. Bubble effects are likely to be a problem for ships with shallow seawater intakes (<5 m) operating in moderate to rough sea states. While a debubbling chamber could be employed to limit this noise, areas with extensive bubble influence in the GTD/optode data are expected to be influenced by bubble injection and exchange in the water column as well, which would still bias the measured $O_2/N_2$.

This method comparison revealed a smoothing of oxygen peaks in the EIMS data, which we attribute to the EIMS equilibrator memory effect. Optode $O_2$ and GTD-based $O_2/N_2$ peaks were much sharper and reached higher maximum values in biological hotspots; in these areas, the observed $O_2/N_2$ was up to 1.5 times greater than $O_2/Ar$. Therefore, in regions with sharp gradients and localized productivity peaks, such as those encountered in this study in the Chirikov basin and the vicinity of Pt. Hope, GTD measurements may more accurately capture absolute productivity values, while EIMS-based observations provide better accuracy in oligotrophic, lower-productivity regions that characterized the rest of the cruise track. On future deployments, EIMS equilibrator response times could also be better optimized by using an equilibrator cartridge with a smaller headspace to water volume ratio, while including a recirculating desiccant loop for constant removal of water vapor in the equilibrator has also been shown to improve response time (Manning et al., 2016).

## 4. Conclusions

This cruise provided a range of conditions under which to assess the efficacy of the GTD/optode system compared to the EIMS for estimating net biological oxygen production. An important takeaway from this method comparison is the relatively quick response time of the GTD, which allows sharp gradients in gas saturation that generally characterize biological hotspots to be well characterized. This method is subject to greater biases from temperature change and bubble injection than the more commonly used $O_2/Ar$ approach. However, we found these biases to be generally small in the Bering and Chukchi Sea during the OS1901 cruise, suggesting the GTD/optode approach may be useful for expanding seasonal observations of productivity in this region. Using historical modeling to approximate $O_2/N_2$' (Izett and Tortell 2021) or utilizing time series measurements on a mooring or drifter that could record the physical changes over time in a given water mass, the expected divergence of $\Delta O_2/N_2$ from $\Delta O_2/Ar$ can be estimated.

The utility of the GTD/optode method depends on the productivity in an area: it is expected to capture large signals in net biological oxygen supersaturation, while oligotrophic areas with low net productivity may be more difficult to determine with certainty. If physical factors influencing solubility are decomposed and accounted for, as Izett and Tortell (2021) do with $O_2/N_2$', the near-equilibrium $\Delta O_2/N_2$ can still be used as an estimate of biological oxygen, with some inherent uncertainty. In this study, $\Delta O_2/N_2$ was typically less than $\Delta O_2/Ar$, which means it likely results in NCP estimates that are slightly underestimated throughout most of the cruise. In regions with very low production, the use of $\Delta O_2/N_2$ could result in occasional instances when an NCP estimate is negative (NCP<0) where $\Delta O_2/Ar$ indicates net autotrophy.

The dependence of $\Delta O_2/N_2$ on calibrated oxygen measurements also needs to be considered when using the GTD/optode method in an autonomous deployment. By incorporating periodic air measurements by the optode, a strategy that has previously been used on floats (Bittig and Körtzinger 2015), reliable oxygen measurements could be maintained throughout a GTD/optode deployment, providing a reference for calibration.

The median value of mixed layer integrated NCP was 9.3 ± 2.8 and 7.9 ± 3.2 mmol $O_2$ $m^{-2}$ $day^{-1}$, based on $O_2/Ar$ and $O_2/N_2$, respectively. The range of NCP was large, from less than zero to >100 mmol $O_2$ $m^{-2}$ $day^{-1}$, with some of the largest NCP estimates measured at well-established hotspots in the Pacific Arctic. The spatial patterns of NCP indicate areas where enhanced mixing may stimulate biological productivity on an intermittent basis, patterns that are difficult to map and monitor with shorter-term incubation-based approaches. Our observations indicate that the GTD/optode method provides promising potential for autonomous observations in the future, which will allow for improved understanding of NCP and the mechanisms driving this production in dynamic environments such as the Pacific Arctic.

## Credit author statement

**Haley Cynar**: Conceptualization, Investigation, Formal Analysis, Writing - Original draft preparation, Visualization; **Laurie Juranek**: Conceptualization, Resources, Writing - Review & Editing, Funding acquisition, Supervision; **Calvin Mordy**: Conceptualization, Resources, Funding acquisition, Writing - Review & Editing; **David Strausz**: Investigation, Data Curation; **Shaun Bell**: Data Curation.

## Declaration of competing interest

The authors declare that they have no known competing financial interests or personal relationships that could have appeared to influence the work reported in this paper.

## Data availability

Data is provided at the Arctic Data Center via links contained in the text.

## Acknowledgements

We thank Sarah Donohoe for her analysis of oxygen samples at sea. We also thank the captain and crew of R/V *Ocean Starr* for their

shipboard support. These data and metadata are available at Arcticdata.io, https://doi.org/10.18739/A2319S41N for underway $O_2$ and $O_2$/Ar, https://doi.org/10.18739/A20R9M539 for discrete $O_2$ and $O_2$/Ar, and https://doi.org/10.18739/A2Z892G7H for $O_2/N_2$. This manuscript is a product of the North Pacific Research Board Arctic Integrated Ecosystem Research Program (https://www.nprb.org/arctic-program; NPRB publication number ArcticIERP-44). This work was supported by NSF awards 1928684 and 1949593 and Simons Foundation Grant 329104 to LWJ. This project is part of the Innovative Technology for Arctic Exploration (ITAE) program funded by NOAA's Pacific Marine Environmental Laboratory (NOAA/PMEL). This publication is partially funded by the Cooperative Institute for Climate, Ocean, & Ecosystem Studies (CIOCES) under NOAA Cooperative Agreement NA20OAR4320271. This is contribution No. 5264 for the Pacific Marine Environmental Laboratory and contribution No. 1146 for CICOES and contribution No. 1011 for NOAA's Ecosystem Fisheries Oceanography Coordinated Investigations.

## Appendix A. Supplementary data

Supplementary data to this article can be found online at https://doi.org/10.1016/j.dsr2.2022.105214.

## References

Andersen, J.K., Andreassen, L.M., Baker, E.H., others, 2020. State of the climate in 2019: the arctic. In: Richter-Menge, J., Druckenmiller, M.L. (Eds.), Bull. Am. Meteorol. Soc., vol. 101, pp. S239–S286. https://doi.org/10.1175/BAMS-D-20-0086.1.

Anderson, L.G., Kaltin, S., 2001. Carbon fluxes in the Arctic Ocean—potential impact by climate change. Polar Res. 20, 225–232. https://doi.org/10.3402/polar.v20i2.6521.

Arrigo, K.R., van Dijken, G.L., 2015. Continued increases in Arctic Ocean primary production. Prog. Oceanogr. 136, 60–70. https://doi.org/10.1016/j.pocean.2015.05.002.

Arrigo, K.R., van Dijken, G., Pabi, S., 2008. Impact of a shrinking Arctic ice cover on marine primary production. Geophys. Res. Lett. 35, 1–6. https://doi.org/10.1029/2008GL035028.

Baker, M.R., Farley, E.V., Danielson, S.L., Mordy, C.W., Stafford, K.M., Dickson, D.M.S., 2022. Integrated research in the arctic – ecosystem linkages and shifts in the northern Bering Sea and eastern and western Chukchi sea. Deep Sea Res. Part II Top. Stud. Oceanogr. 206. In this issue.

Baker, M.R., Farley, E.V., Ladd, C., Danielson, S.L., Stafford, K.M., Huntington, H.P., Dickson, D.M.S., 2020. Integrated ecosystem research in the Pacific Arctic – understanding ecosystem processes, timing and change. Deep Sea Res. Part II Top. Stud. Oceanogr. 177, 104850 https://doi.org/10.1016/j.dsr2.2020.104850.

Bélanger, S., Babin, M., Tremblay, J.-É., 2013. Increasing cloudiness in Arctic damps the increase in phytoplankton primary production due to sea ice receding. Biogeosciences 10, 4087–4101. https://doi.org/10.5194/bg-10-4087-2013.

Benson, B.B., Krause, D., 1984. The concentration and isotopic fractionation of oxygen dissolved in freshwater and seawater in equilibrium with the atmosphere1. Limnol. Oceanogr. 29, 620–632. https://doi.org/10.4319/lo.1984.29.3.0620.

Bittig, H.C., Körtzinger, A., 2015. Tackling oxygen optode drift: near-surface and in-air oxygen optode measurements on a float provide an accurate in situ reference. J. Atmos. Ocean. Technol. 32, 1536–1543. https://doi.org/10.1175/JTECH-D-14-00162.1.

Bittig, H.C., Körtzinger, A., Neill, C., others, 2018. Oxygen optode sensors: principle, characterization, calibration, and application in the ocean. Front. Mar. Sci. 4, 1–25. https://doi.org/10.3389/fmars.2017.00429.

Bushinsky, S.M., Emerson, S.R., Riser, S.C., Swift, D.D., 2016. Accurate oxygen measurements on modified argo floats using in situ air calibrations. Limnol Oceanogr. Methods 14, 491–505. https://doi.org/10.1002/lom3.10107.

Carmack, E.C., Wassmann, P., 2006. Food webs and physical–biological coupling on pan-Arctic shelves: unifying concepts and comprehensive perspectives. Prog. Oceanogr. 71, 446–477. https://doi.org/10.1016/j.pocean.2006.10.004.

Carmack, E., Polyakov, I., Padman, L., others, 2015. Toward quantifying the increasing role of oceanic heat in sea ice loss in the new arctic. Bull. Am. Meteorol. Soc. 96, 2079–2105. https://doi.org/10.1175/BAMS-D-13-00177.1.

Carpenter, J.H., 1965. The accuracy of the winkler method for dissolved oxygen analysis. Limnol. Oceanogr. 10, 135–140. https://doi.org/10.4319/lo.1965.10.1.0135.

Cassar, N., Barnett, B.A., Bender, M.L., Kaiser, J., Hamme, R.C., Tilbrook, B., 2009. Continuous high-frequency dissolved O 2/Ar measurements by equilibrator inlet mass spectrometry. Anal. Chem. 81, 1855–1864. https://doi.org/10.1021/ac802300u.

Codispoti, L.A., Kelly, V., Thessen, A., Matrai, P., Suttles, S., Hill, V., Steele, M., Light, B., 2013. Synthesis of primary production in the Arctic Ocean: III. Nitrate and phosphate based estimates of net community production. Prog. Oceanogr. 110, 126–150. https://doi.org/10.1016/j.pocean.2012.11.006.

Craig, H., Hayward, T., 1987. Oxygen supersaturation in the ocean: biological versus physical contributions. Science 80 (235), 199–202. https://doi.org/10.1126/science.235.4785.199.

Danielson, S.L., Ahkinga, O., Ashjian, C., others, 2020. Manifestation and consequences of warming and altered heat fluxes over the Bering and Chukchi Sea continental shelves. Deep. Res. Part II Top. Stud. Oceanogr. 177 https://doi.org/10.1016/j.dsr2.2020.104781.

Danielson, S.L., Eisner, L., Ladd, C., Mordy, C.W., Sousa, L., Weingartner, T.J., 2017. A comparison between late summer 2012 and 2013 water masses, macronutrients, and phytoplankton standing crops in the northern Bering and Chukchi Seas. Deep. Res. Part II Top. Stud. Oceanogr. 135, 7–26. https://doi.org/10.1016/j.dsr2.2016.05.024.

DeGrandpre, M., Evans, W., Timmermans, M.L., Krishfield, R., Williams, B., Steele, M., 2020. Changes in the Arctic ocean carbon cycle with diminishing ice cover. Geophys. Res. Lett. 47 https://doi.org/10.1029/2020GL088051.

Emerson, S.R., Stump, C., Johnson, B., Karl, D.M., 2002. In situ determination of oxygen and nitrogen dynamics in the upper ocean. Deep-Sea Res. Part I Oceanogr. Res. Pap. 49, 941–952. https://doi.org/10.1016/S0967-0637(02)00004-3.

Emerson, S.R., Stump, C., Nicholson, D.P., 2008. Net biological oxygen production in the ocean: remote in situ measurements of O 2 and N 2 in surface waters. Global Biogeochem. Cycles 22. https://doi.org/10.1029/2007GB003095 n/a-n/a.

Emerson, S.R., Yang, B., White, M., Cronin, M., 2019. air-sea gas transfer: determining bubble fluxes with in situ N2 observations. J. Geophys. Res. Ocean. 124, 2716–2727. https://doi.org/10.1029/2018JC014786.

Eveleth, R., Cassar, N., Sherrell, R.M., Ducklow, H., Meredith, M.P., Venables, H.J., Lin, Y., Li, Z., 2017. Ice melt influence on summertime net community production along the Western Antarctic Peninsula. Deep. Res. Part II Top. Stud. Oceanogr. 139, 89–102. https://doi.org/10.1016/j.dsr2.2016.07.016.

Eveleth, R., Timmermans, M.L., Cassar, N., 2014. Physical and biological controls on oxygen saturation variability in the upper Arctic Ocean. J. Geophys. Res. Ocean. 119, 7420–7432. https://doi.org/10.1002/2014JC009816.

Garcia, H.E., Gordon, L.I., 1992. Oxygen solubility in seawater: better fitting equations. Limnol. Oceanogr. 37, 1307–1312. https://doi.org/10.4319/lo.1992.37.6.1307.

Glueckauf, E., 1951. The composition of atmospheric air. In: Compendium of Meteorology. American Meteorological Society, pp. 3–10.

Grebmeier, J.M., Bluhm, B.A., Cooper, L.W., others, 2015. Ecosystem characteristics and processes facilitating persistent macrobenthic biomass hotspots and associated benthivory in the Pacific Arctic. Prog. Oceanogr. 136, 92–114. https://doi.org/10.1016/j.pocean.2015.05.006.

Grebmeier, J.M., Cooper, L.W., Feder, H.M., Sirenko, B.I., 2006. Ecosystem dynamics of the pacific-influenced northern bering and Chukchi seas in the Amerasian arctic. Prog. Oceanogr. 71, 331–361. https://doi.org/10.1016/j.pocean.2006.10.001.

Grebmeier, J.M., Moore, S.E., Overland, J.E., Frey, K.E., Gradinger, R., 2010. Biological response to recent pacific arctic sea ice retreats. Eos, Trans. Am. Geophys. Union 91, 161. https://doi.org/10.1029/2010EO180001.

Hamme, R.C., Berry, J.E., Klymak, J.M., Denman, K.L., 2015. In situ O2 and N2 measurements detect deep-water renewal dynamics in seasonally-anoxic Saanich Inlet. Continent. Shelf Res. 106, 107–117. https://doi.org/10.1016/j.csr.2015.06.012.

Hamme, R.C., Cassar, N., Lance, V.P., others, 2012. Dissolved O2/Ar and other methods reveal rapid changes in productivity during a Lagrangian experiment in the Southern Ocean. J. Geophys. Res. Ocean. 117, 1–19. https://doi.org/10.1029/2011JC007046.

Hamme, R.C., Emerson, S.R., 2004. The solubility of neon, nitrogen and argon in distilled water and seawater. Deep. Res. Part I Oceanogr. Res. Pap. 51, 1517–1528. https://doi.org/10.1016/j.dsr.2004.06.009.

Hamme, R.C., Emerson, S.R., 2006. Constraining bubble dynamics and mixing with dissolved gases: implications for productivity measurements by oxygen mass balance. J. Mar. Res. 64, 73–95. https://doi.org/10.1357/002224006776412322.

Hamme, R.C., Nicholson, D.P., Jenkins, W.J., Emerson, S.R., 2019. Using noble gases to assess the ocean's carbon pumps. Ann. Rev. Mar. Sci 11, 75–103. https://doi.org/10.1146/annurev-marine-121916-063604.

Harada, N., 2016. Review: potential catastrophic reduction of sea ice in the western Arctic Ocean: its impact on biogeochemical cycles and marine ecosystems. Global Planet. Change 136, 1–17. https://doi.org/10.1016/j.gloplacha.2015.11.005.

Hendricks, M.B., Bender, M.L., Barnett, B.A., 2004. Net and gross O2 production in the southern ocean from measurements of biological O2 saturation and its triple isotope composition. Deep. Res. Part I Oceanogr. Res. Pap. 51, 1541–1561. https://doi.org/10.1016/j.dsr.2004.06.006.

Hood, E.M., 1998. Characterization of Air-Sea Gas Exchange Processes and Dissolved Gas/Ice Interactions Using Noble Gases. Massachusetts Institute of Technology & Woods Hole Oceanographic Institution.

Hood, E.M., Howes, B.L., Jenkins, W.J., 1998. Dissolved gas dynamics in perennially ice-covered Lake Fryxell, Antarctica. Limnol. Oceanogr. 43, 265–272. https://doi.org/10.4319/lo.1998.43.2.0265.

Izett, R.W., 2021. O2N2 NCP Toolbox. https://doi.org/10.5281/zenodo.4024925.

Izett, R.W., Hamme, R.C., McNeil, C.L., Manning, C.C., Bourbonnais, A., Tortell, P., 2021. ΔO2/N2' as a new tracer of marine net community production: application and evaluation in the Subarctic Northeast Pacific and Canadian Arctic Ocean. Front. Mar. Sci. 8. https://doi.org/10.3389/fmars.2021.718625.

Izett, R.W., Tortell, P., 2020. The pressure of in situ gases instrument (PIGI) for autonomous shipboard measurement of dissolved O2 and N2 in surface ocean waters. Oceanography 33. https://doi.org/10.5670/oceanog.2020.214.

Izett, R.W., Tortell, P.D., 2021. ΔO2/N2′ as a tracer of mixed layer net community production: theoretical considerations and proof-of-concept. Limnol Oceanogr. Methods 19, 497–509. https://doi.org/10.1002/lom3.10440.

Juranek, L.W., Quay, P.D., 2005. In vitro and in situ gross primary and net community production in the North Pacific Subtropical Gyre using labeled and natural abundance isotopes of dissolved O 2. Global Biogeochem. Cycles 19, 1–15. https://doi.org/10.1029/2004GB002384.

Juranek, L.W., Quay, P.D., 2010. Basin-wide photosynthetic production rates in the subtropical and tropical Pacific Ocean determined from dissolved oxygen isotope ratio measurements. Global Biogeochem. Cycles 24. https://doi.org/10.1029/2009GB003492 n/a-n/a.

Juranek, L.W., Quay, P.D., Feely, R.A., Lockwood, D., Karl, D.M., Church, M.J., 2012. Biological production in the NE Pacific and its influence on air-sea CO 2 flux: evidence from dissolved oxygen isotopes and O 2/Ar. J. Geophys. Res. Ocean. 117 https://doi.org/10.1029/2011JC007450.

Juranek, L.W., Takahashi, T., Mathis, J.T., Pickart, R.S., 2019. Significant biologically mediated CO 2 uptake in the pacific arctic during the late open water season. J. Geophys. Res. Ocean. 124, 1–23. https://doi.org/10.1029/2018JC014568.

Kaiser, J., Reuer, M.K., Barnett, B.A., Bender, M.L., 2005. Marine productivity estimates from continuous O 2/Ar ratio measurements by membrane inlet mass spectrometry. Geophys. Res. Lett. 32 https://doi.org/10.1029/2005GL023459.

Laws, E.A., 1991. Photosynthetic quotients, new production and net community production in the open ocean. Deep-Sea Res., Part A 38, 143–167. https://doi.org/10.1016/0198-0149(91)90059-O.

Lewis, K.M., Van Dijken, G.L., Arrigo, K.R., 2020. Changes in phytoplankton concentration now drive increased Arctic Ocean primary production. Science 80 (369), 198–202. https://doi.org/10.1126/science.aay8380.

Lockwood, D., Quay, P.D., Kavanaugh, M.T., Juranek, L.W., Feely, R.A., 2012. High-resolution estimates of net community production and air-sea CO 2 flux in the northeast Pacific. Global Biogeochem. https://doi.org/10.1029/2012GB004380. Cycles **26**.

Manning, C.C., Stanley, R.H.R., Lott, D.E., 2016. Continuous measurements of dissolved Ne, Ar, Kr, and Xe ratios with a field-deployable gas equilibration mass spectrometer. Anal. Chem. 88, 3040–3048. https://doi.org/10.1021/acs.analchem.5b03102.

Mathis, J.T., Bates, N.R., Hansell, D.A., Babila, T., 2009. Net community production in the northeastern Chukchi Sea. Deep Sea Res. Part II Top. Stud. Oceanogr. 56, 1213–1222. https://doi.org/10.1016/j.dsr2.2008.10.017.

McNeil, C.L., Johnson, B.D., Farmer, D.M., 1995. In-situ measurement of dissolved nitrogen and oxygen in the ocean. Deep. Res. Part I 42, 819–826. https://doi.org/10.1016/0967-0637(95)97829-W.

McNeil, C.L., Katz, D., Wanninkhof, R., Johnson, B., 2005. Continuous shipboard sampling of gas tension, oxygen and nitrogen. Deep. Res. Part I Oceanogr. Res. Pap. 52, 1767–1785. https://doi.org/10.1016/j.dsr.2005.04.003.

Mesinger, F., DiMego, G., Kalnay, E., others, 2006. North American regional reanalysis. Bull. Am. Meteorol. Soc. 87, 343–360. https://doi.org/10.1175/BAMS-87-3-343.

Mordy, C.W., Bell, S., Cokelet, E.D., others, 2020. Seasonal and interannual variability of nitrate in the eastern Chukchi Sea: transport and winter replenishment. Deep. Res. Part II Top. Stud. Oceanogr. 177, 104807 https://doi.org/10.1016/j.dsr2.2020.104807.

Mordy, C.W., Eisner, L., Kearney, K., others, 2021. Spatiotemporal variability of the nitrogen deficit on the eastern Bering Sea shelf. Continent. Shelf Res. 224, 104423 https://doi.org/10.1016/j.csr.2021.104423.

NASA Goddard Space Flight Group, Ocean Ecology Laboratory, Ocean Biology Processing Group, Moderate-resolution Imaging Spectroradiometer (MODIS) Aqua Chlorophyll Data, 2018. Reprocessing. NASA OB. DAAC, Greenbelt, MD, USA data/10.5067/AQUA/MODIS/L3M/CHL/2018.

Padin, X.A., Vázquez-Rodríguez, M., Rios, A.F., Pérez, F.F., 2007. Atmospheric CO2 measurements and error analysis on seasonal air-sea CO2 fluxes in the Bay of Biscay. J. Mar. Syst. 66, 285–296. https://doi.org/10.1016/j.jmarsys.2006.05.010.

Reuer, M.K., Barnett, B.A., Bender, M.L., Falkowski, P.G., Hendricks, M.B., 2007. New estimates of Southern Ocean biological production rates from O2/Ar ratios and the triple isotope composition of O2. Deep-Sea Res. Part I Oceanogr. Res. Pap. 54, 951–974. https://doi.org/10.1016/j.dsr.2007.02.007.

Semiletov, I., Makshtas, A., Akasofu, S.-I., Andreas, E.L., 2004. Atmospheric CO 2 balance: the role of Arctic sea ice. Geophys. Res. Lett. 31 https://doi.org/10.1029/2003GL017996 n/a-n/a.

Serreze, M.C., Stroeve, J., 2015. Arctic sea ice trends, variability and implications for seasonal ice forecasting. Philos. Trans. R. Soc. A Math. Phys. Eng. Sci. 373 https://doi.org/10.1098/rsta.2014.0159.

Shiozaki, T., Fujiwara, A., Ijichi, M., Harada, N., Nishino, S., Nishi, S., Nagata, T., Hamasaki, K., 2018. Diazotroph community structure and the role of nitrogen fixation in the nitrogen cycle in the Chukchi Sea (western Arctic Ocean). Limnol. Oceanogr. 63, 2191–2205. https://doi.org/10.1002/lno.10933.

Song, H., Ji, R., Jin, M., Li, Y., Feng, Z., Varpe, Ø., Davis, C.S., 2021. Strong and regionally distinct links between ice-retreat timing and phytoplankton production in the Arctic Ocean. Limnol. Oceanogr. 66, 1–11. https://doi.org/10.1002/lno.11768.

Stammerjohn, S., Massom, R., Rind, D., Martinson, D., 2012. Regions of rapid sea ice change: An inter-hemispheric seasonal comparison. Geophys. Res. Lett. 39, 1–8. https://doi.org/10.1029/2012GL050874.

Stanley, R.H.R., Kirkpatrick, J.B., Cassar, N., Barnett, B.A., Bender, M.L., 2010. Net community production and gross primary production rates in the western equatorial Pacific. Global Biogeochem. https://doi.org/10.1029/2009GB003651. Cycles **24**.

Stroeve, J., Meier, W.N., 2018. Sea Ice Trends and Climatologies from SMMR and SSM/I-SSMIS. Version 3. https://doi.org/10.5067/IJ0T7HFHB9Y6.

Teeter, L., Hamme, R.C., Ianson, D., Bianucci, L., 2018. Accurate estimation of net community production from O2/Ar measurements. Global Biogeochem. Cycles 32, 1163–1181. https://doi.org/10.1029/2017GB005874.

Thomson, J., Rogers, W.E., 2014. Swell and Sea in the emerging Arctic ocean. Geophys. Res. Lett. 41, 3136–3140. https://doi.org/10.1002/2014GL059983.

Toole, J.M., Timmermans, M.L., Perovich, D.K., Krishfield, R.A., Proshutinsky, A., Richter-Menge, J.A., 2010. Influences of the ocean surface mixed layer and thermohaline stratification on Arctic Sea ice in the central Canada Basin. J. Geophys. Res. Ocean. 115, 1–14. https://doi.org/10.1029/2009JC005660.

Tremblay, J.-É., Gagnon, J., 2009. The effects of irradiance and nutrient supply on the productivity of Arctic waters: a perspective on climate change. Influ. Clim. Chang. Chang. Arct. Sub-Arctic Cond. 73–93. https://doi.org/10.1007/978-1-4020-9460-6_7.

Tremblay, J.É., Anderson, L.G., Matrai, P., Coupel, P., Bélanger, S., Michel, C., Reigstad, M., 2015. Global and regional drivers of nutrient supply, primary production and CO2 drawdown in the changing Arctic Ocean. Prog. Oceanogr. 139, 171–196. https://doi.org/10.1016/j.pocean.2015.08.009.

Tremblay, J.É., Bélanger, S., Barber, D.G., others, 2011. Climate forcing multiplies biological productivity in the coastal Arctic Ocean. Geophys. Res. Lett. 38, 2–6. https://doi.org/10.1029/2011GL048825.

Trull, T.W., Jansen, P., Schulz, E., Weeding, B., Davies, D.M., Bray, S.G., 2019. Autonomous multi-trophic observations of productivity and export at the Australian southern ocean time series (SOTS) reveal sequential mechanisms of physical-biological coupling. Front. Mar. Sci. 6, 1–17. https://doi.org/10.3389/fmars.2019.00525.

Wanninkhof, R., 2014. Relationship between wind speed and gas exchange over the ocean revisited. Limnol Oceanogr. Methods 12, 351–362. https://doi.org/10.4319/lom.2014.12.351.

Wassmann, P., Reigstad, M., 2011. Future Arctic ocean seasonal ice zones and implications for pelagic-benthic coupling. Oceanography 24, 220–231. https://doi.org/10.5670/oceanog.2011.74.

Weeding, B., Trull, T.W., 2014. Hourly oxygen and total gas tension measurements at the Southern Ocean Time Series site reveal winter ventilation and spring net community production. J. Geophys. Res. Ocean. 119, 348–358. https://doi.org/10.1002/2013JC009302.

Weiss, R.F., Price, B.A., 1980. Nitrous oxide solubility in water and seawater. Mar. Chem. 8, 347–359. https://doi.org/10.1016/0304-4203(80)90024-9.

Woolf, D.K., Thorpe, S.A., 1991. Bubbles and the air-sea exchange of gases in near-saturation conditions. J. Mar. Res. 49, 435–466. https://doi.org/10.1357/002224091784995765.

Zankel, K.L., Reed, D.W., Clayton, R.K., 1968. Fluorescence and photochemical quenching in photosynthetic reaction centers. Proc. Natl. Acad. Sci. U. S. A 61, 1243–1249. https://doi.org/10.1073/pnas.61.4.1243.